

Author response to Reviewer 1

We thank David Sugden for his review of the manuscript and his insightful comments.

Below, we address referee comments and describe additional, unsolicited changes that we've made to improve the manuscript. Referee comments are supplied in bold, with our responses in regular text.

Specific comments:

1. Is it possible that some of the moraines near the ice margin are ice-cored? Are any of these moraines stranded blue-ice moraines? If so, could subsequent ablation help explain some outliers? Bearing in mind the blue ice moraines at high altitudes in the TAM, it would be good to hear your view on this.

Although we recognize that the blue-ice moraine model is important at high elevation sites throughout the TAM, our field observations suggest that moraines at Roberts Massif are not stranded blue-ice moraines. In general, we characterize the moraines at Roberts Massif as boulder belt moraines, associated with thin drifts of angular boulders and directly overlying bedrock in several locations. Furthermore, the present ice fronts facing the moraine complexes are convex, have minimal debris within the ice, and do not have accumulating debris fields. These observations, coupled with the absence of modern blue-ice moraines at Roberts Massif, suggest that sediment supply to the glacier is low, which is inconsistent with blue-ice moraines forming at other TAM locations today. While we do not interpret the Roberts Massif moraines as stranded blue-ice moraines, we acknowledge that (at least some) young outliers in our cosmogenic-nuclide dataset may result from ablation of a small ice core from moraines, and have added a sentence on this topic on lines 466-467 and a parenthetical reference on line 472.

2. The start of the discussion is the place where you reference studies implying the presence of grounded ice in the Ross and its effect in blocking the flow of Transantarctic outlet glaciers. Later you make this an argument for the stability of the West Antarctic ice sheet for 15 Ma. Could you describe the evidence that the upper parts of Shackleton Glacier are affected by conditions near its convergence with Ross Sea ice? Once established for the reader, then the argument is strong. I was of the belief that there was little change higher up the transverse glaciers

We agree that this argument needed clarification. Previous studies have shown that buttressing by Ross Sea ice affects ice thickness at the heads of TAM outlet glaciers, albeit significantly less thickening than at the mouths of these glaciers. To further our argument, we've updated the paragraph on lines 534-544 to include references that evidence the effect of buttressing ice in the Ross Sea on the uppermost reaches of TAM glaciers. Because the moraines at Roberts Massif mark times when the ice configuration was similar to today, we speculate that there was at least a buttressing ice shelf in the Ross Sea, or even a grounded ice sheet. Either of these scenarios would require inflow of ice to the Ross Sea from West Antarctica. However, we recognize that we cannot distinguish between a Ross Ice Shelf (ice configuration in the Ross Sea similar to today) and a Ross Ice Sheet (ice configuration similar to the Last Glacial Maximum) with our data. Therefore, we've also updated the paragraph on lines 534-544 and the final sentence of the paper on lines 690-693 to allow for either of these possibilities.

3. Lines 546-553. Origin of debris from the base. Reference here the direct evidence of basal freezing near Mt Archernar? Eg. Bader et al, 2016, Q.S.R. and Graly et al. 2018, J.Glac. This seems more significant than reference to a general continental scale model.

References to Bader et al. (2016) and Graly et al. (2018) added.

4. Ditto Uplift. Reference a fundamental paper on flexural uplift eg Stern & Tenbrink, JGR, 1989, 94, p.10315?

Reference to Stern and Ten Brink (1989) added.

Technical corrections:

1. Fig 3 and caption. I found the labels on the Figure and the caption confusing. For example, where is B? And (b) seems to describe the highlighted area in A'. What does (c) show?

We've clarified the inset labels in both the figure and the caption.

2. Fig 8 and caption. Explain what 8c shows? Southwest Col drift not explicitly shown on the figure.

We've added the word "drift" to the Southwest Col label in Figure 8a and 8b, and bolded it for clarity. We also added a description of inset c, which does not show the Southwest Col drift, to the figure caption.

Additional changes to the manuscript:

1. We correct a miscount in total sample numbers found in the original submission, which included samples from the Supplementary Information that are not critical to the interpretations discussed in the text. Thus, we revise the total number of samples discussed in the text from 180 to 168 on lines 13 and 70, as well as the breakdown of cosmogenic-nuclide measurements on lines 392-393.
2. Removed a stray '---' from line 489.
3. Changed erroneous section reference to Section 4.1 on line 529 to the correct Section 3.1.

Author response to Reviewer 2

We thank Julia Lindow for her thorough review of the manuscript and her insightful comments.

Below, we address referee comments and describe additional, unsolicited changes that we've made to improve the manuscript. Referee comments are supplied in bold, with our responses in regular text.

Specific comments:

1. Based on the detailed description of field work and sampling, the authors put a great deal of effort into sample selection and documentation, especially to minimize effects of common complications in surface exposure dating, e.g. nuclide inheritance or non-cosmogenic nuclides. So mainly out of curiosity, could some boulders of sufficient size have provided shielded samples to get direct measurements of inherited / non- cosmogenic nuclides in combination with the surface samples?

We did not collect samples shielded by larger boulders or from the undersides of boulders, although recognize that this technique may be of use for quantifying inherited and/or non-cosmogenic nuclides (e.g., Valletta et al., 2017). However, on lines 148–153 of the manuscript, we discuss previous estimates of non-cosmogenic ^3He in Ferrar dolerite, noting that these values are within measurement error for our samples.

2. No potential shielding from snow cover is discussed, and I assume it is considered negligible in respect to locality and the known average low snow accumulation. However, the age of the samples allows for some degree of uncertainty on seasonal or prolonged snow cover, and I would be interested to hear the authors thoughts on this.

As this comment suggests, significant persistent snow cover is inconsistent with local climatology, extremely low subaerial erosion rates over the last 15 Ma, and salt accumulation in TAM soils. Further, the observation that Roberts Massif is a long-term ablation area, as evidenced by the surrounding modern blue-ice ablation zones and the abundant moraines (especially younger than 3 Ma) throughout the massif, supports the idea of low snow accumulation at this location. Given these observations, we've made the assumption that a snow cover correction is not necessary over the course of our record, despite the old age of the landforms.

3. Line 269-271: "First described by Mercer (1972), the Sirius Group occurs throughout the upper (> ~2000 m elevation) TAM as erosional remnants of clay-rich diamicton that are correlated with at least one period of past temperate glaciation." I read this as Sirius deposits are exclusively found above 2000 m, which could be misleading because there are Sirius Group outcrops are at lower elevations, e.g. Hambrey et al., 2003, and Mayewski 1975. I suggest changing the statement to > ~1500 m.

We've updated the text accordingly.

4. Line 571: " \leq ~200m", this is a little odd, I would just write $<$ ~200 m.

We've changed the text to read $<$ ~200 m.

5. Section 4.1, Uplift at Roberts Massif: I understand the notion to compare potential uplift rates with existing data (here McMurdo Dry Valleys). However, I question the reliability of evaluating uplift rates or isostatic rebound over the extend of almost 1000 km, and thereby neglecting the influence of regional morphology and geologic structures. For me, the argumentation implies the whole TAM behaved as one block, undisturbed from north to south, while trough incision driven by glacial erosion (as discussed to be the main driver of uplift at Roberts Massif) can also (re-)activate underlying faults and induce block uplift (e.g. Studinger et al. 2006, or as shown for the Shackleton Range: Paxman et al., 2017). This would reflect in localized uplift rates which could be

very different from the McMurdo Dry Valleys. I think this section would benefit from additional details on uplift along the TAM (e.g. Paxman et al., 2019).

We acknowledge the importance of the hypothesis that different TAM blocks have different uplift histories over the last 15 Ma. However, our data do not provide evidence for or against that hypothesis, but rather place bounds on the allowable amount of uplift at Roberts Massif over the course of our record. Given this, we don't discuss differential uplift across the TAM in this paper, but provide evidence for uplift rates elsewhere in the TAM for completeness.

Technical corrections:

1. Fig 1 and 3: missing scale bar and Lat/Lon labels (Fig 1), also, if possible, highlight/mark study area in figure 1.

We've added a scale bar, lat/long labels, and a box highlighting the study area to for Figure 1. For Figure 3, we've included dimensions in the caption.

2. Fig 4, caption: no mention of (d) in the caption and missing reference to (d) under a); see : "...with numbers corresponding to moraine names in (c) and letters A and A' corresponding to positions in (c)."

We've added a description of and reference to panel (d) to the caption and further updated the caption for clarity.

3. Fig 5 (b), caption: It would be interesting to know the length of the pole for better scale or just give an approximate thickness.

The caption now includes the pole length (120 cm).

4. Fig 11: text and axis labels are quite small, and rather hard to read.

All font sizes will be revisited for final production files.

5. Fig 12: Please check numbering for BBY, BGE and WAL, it's different in figure 4. Also in the map (Fig 4) it is not quite clear which one is BGE.

The labels for BGE and WAL were erroneously switched in Figure 12. This has been corrected. Information about the NLO/NLI and POS moraine complexes, and clarification about the BBY and BGE moraines has also been added to the caption.

6. Fig 14, caption: (c) is missing, and as a consequence subsequent description is off by one letter. "Colors on the timescale at the bottom correspond to moraine colors in Figures 4, 7, and 8." They don't, at least not for the reader, e.g. 'Pliocene' is more yellow then the orange of the moraines in the overview figures. Also, the color scheme used for the age data (d) implies a relation to the timescale used, which I find a little confusing. Maybe a different set of colors or symbols could make this figure clearer.

We've corrected the panel references in the caption. To avoid confusion with the timescale color bar, we've removed these colors altogether as well as the reference to Figures 4, 7, and 8. Finally, we added a legend to panel d, rather than listing the colors in the figure caption, to improve clarity.

7. For the figures in general: The marker and information overlaying satellite maps are of mediocre quality/readability, which might be the result of compressing the images for this pre-print version, if not it would be worth looking into to ensure good quality images in the final version.

We will ensure that the final version includes print-quality images.

Additional changes to the manuscript:

1. Numbers were switched for the WBK and POS moraines in Figure 4. This has been corrected.
2. Corrected erroneous section references on lines 509 and 524.
3. Corrected erroneous figure references on lines 505, 513, 519, 584, and 603.
4. Clarified figure reference location in sentence on lines 332–335.

Author Response to Editor Comments

In addition to the manuscript changes outlined in our responses to reviewers, the following changes have been made to the manuscript to improve clarity. These updates can be seen in the revised manuscript below.

Line 91: archive changed to database.

All instances of “basemap” have been changed to base map.

Figure 2 caption updated to reflect labeled panels. Changed “e.g.” to “i.e.”

Figures 1 and 3: we added a scale bar to Figure 1, as suggested by Julia Lindow. In Figure 1, we also denoted the view of in Figure 3. However, we did not include dimensions in Figure 3, as those were not provided with the aerial imagery. We believe these changes are sufficient for describing the scale of Roberts Massif as shown in Figure 3.

1 **A 14.5 million-year record of East Antarctic Ice Sheet**
2 **fluctuations from the central Transantarctic Mountains,**
3 **constrained with cosmogenic ^3He , ^{10}Be , ^{21}Ne , and ^{26}Al**

4 Allie Balter^{1,2}, Gordon Bromley^{2,3}, Greg Balco⁴, Holly Thomas¹, Margaret S. Jackson³

5 ¹School of Earth and Climate Sciences, University of Maine, Orono, Maine, USA

6 ²Climate Change Institute, University of Maine, Orono, Maine, USA

7 ³Geography, National University of Ireland, Galway, Ireland

8 ⁴Berkeley Geochronology Center, Berkeley, California, USA

9 *Correspondence to: Allie Balter (abalter@ldeo.columbia.edu)*

10 **Abstract.** The distribution of moraines in the Transantarctic Mountains affords direct constraint of past ice-marginal
11 positions of the East Antarctic Ice Sheet (EAIS). Here, we describe glacial-geologic observations and cosmogenic-
12 nuclide exposure ages from Roberts Massif, an ice-free area in the central Transantarctic Mountains. We measured
13 cosmogenic ^3He , ^{10}Be , ^{21}Ne , and ^{26}Al in 168 dolerite and sandstone boulders collected from 24 distinct deposits. Our
14 data show that a cold-based EAIS was present, in a configuration similar to today, for many periods over the last ~14.5
15 Myr, including the mid-Miocene, Late Pliocene, and early-to-mid Pleistocene. Moraine ages at Roberts Massif
16 increase with distance from, and elevation above the modern ice margin, which is consistent with a persistent EAIS
17 extent during glacial maxima, and slow, isostatic uplift of the massif itself in response to trough incision by outlet
18 glaciers. We also employ the exceptionally high cosmogenic-nuclide concentrations in several boulders, along with
19 multi-isotope measurements in sandstone boulders, to infer extremely low erosion rates ($\ll 5$ cm/Myr) over the period
20 covered by our record. Although our data are not a direct measure of ice volume, the Roberts Massif glacial record
21 indicates that the EAIS was present and similar to its current configuration during at least some periods when global
22 temperature was believed to be warmer and/or atmospheric CO_2 concentrations were likely higher than today.

Deleted: 80

23 **1 Introduction**

24 In this paper, we describe glacial deposits preserved in the central Transantarctic Mountains (TAM, Figure 1) that
25 provide unambiguous evidence for the presence of the East Antarctic Ice Sheet (EAIS), in a configuration similar to
26 today, for periods of the middle Miocene, late Pliocene, and early to middle Pleistocene. Our chronology therefore
27 provides geologic targets for ice volume reconstructions derived from marine proxy records and sea-level estimates.
28 Current estimates of pre-Pleistocene EAIS ice volume are based largely on $\delta^{18}\text{O}$ of benthic foraminifera (e.g.,
29 Shevenell et al., 2008), which primarily records global temperature and ice volume, and farfield sea-level indicators
30 (e.g., Miller et al., 2005), such as raised shorelines (e.g., Rovere et al., 2014). These proxy records (e.g., Holbourn et
31 al., 2013), along with stratigraphic evidence from ice proximal sediment cores (Levy et al., 2016) and modeling studies
32 (Gasson et al., 2016), suggest that during the middle Miocene the EAIS oscillated between states both larger and

34 smaller than present in response to fluctuations in CO₂ and temperature. After ~14 Ma, such proxy records suggest
35 general presence of the EAIS, but with potentially significant retreat during past warm periods, such as the mid-
36 Pliocene Warm Period (3.3–3.0 Ma) (e.g., Dutton et al., 2015 and references therein), when temperatures are thought
37 to have been 2–3°C warmer than preindustrial (Haywood et al., 2013) and CO₂ was ~400 ppm (Pagani et al., 2010;
38 Seki et al., 2010). Although valuable for elucidating long-term trends in sea-level change, these proxy records do not
39 directly record the volume of specific ice sheets. In contrast, glacial deposits from ice-free areas of Antarctica itself
40 provide direct geologic evidence for past ice sheet variability.

41 Previous geomorphic and glacial chronologic studies in the Transantarctic Mountains (TAM), a ~3000 km-long
42 topographic barrier through which outlet glaciers of the EAIS drain into the Ross Sea Embayment (Figure 1), suggest
43 the presence of pre-Pleistocene glacial deposits. Two distinct categories of deposits characterize the Antarctic glacial-
44 geologic record: basal tills of the Sirius Group (e.g., Mayewski, 1975; Mercer, 1972), which indicate at least one
45 period of temperate glaciation, and thin, bouldery drifts and moraines deposited by ice frozen to the bed (e.g., Prentice
46 et al., 1986), which overlie the older temperate deposits. In southern Victoria Land, Schaefer et al., (1999) reported a
47 minimum age of > 10 Ma for Sirius Group tills at Mt. Fleming. Similarly, relict subglacial flood deposits in the
48 Coombs Hills resulting from wet-based glaciation afford ³He ages between ~8.5 and 10.5 Ma, assuming zero erosion,
49 and as much as ~15 Ma if erosion rates of 0.03–0.06 m/Ma are applied (Margerison et al., 2005). In the same region,
50 ⁴⁰Ar/³⁹Ar ages on in situ ash layers interbedded with cold-based ablation tills in the Asgard Range date the transition
51 from temperate to polar glaciation to between 15 and 13.6 Ma (Sugden and Denton, 2004). The preservation of such
52 deposits over the last ~15 Ma has been invoked as evidence for persistent polar desert conditions, and by extension
53 the presence of the EAIS, since that time (Denton et al., 1993).

54 Chronologic constraints on the overlying cold-based deposits come primarily from surface-exposure dating, which
55 has been employed at several locations throughout the TAM, including southern Victoria Land (Brook et al., 1995,
56 1993; Brown et al., 1991; Bruno et al., 1997; Ivy-Ochs et al., 1995; Strasky et al., 2009); Beardmore (Ackert and Kurz,
57 2004) and Law (Kaplan et al., 2017) Glaciers in the central TAM; and Scott (Spector et al., 2017) and Reedy (Bromley
58 et al., 2010; Todd et al., 2010) Glaciers in the southern TAM. Approximately 30 previously published exposure ages
59 (see ICE-D:ANTARCTICA online [database: http://antarctica.ice-d.org](http://antarctica.ice-d.org)) indicate the preservation of cold-based glacial
60 landforms in Antarctica that are at least 5 Ma in age. For example, a prominent boulder moraine in the Dominion
61 Range, upper Beardmore Glacier, was dated with ³He to 5.2 Ma (Ackert and Kurz, 2004). Similarly, ¹⁰Be ages from
62 erratic boulders at Reedy Glacier suggest deposition of the ‘Reedy E drift’ at > ~5 Ma (Bromley et al., 2010).

Deleted: archive

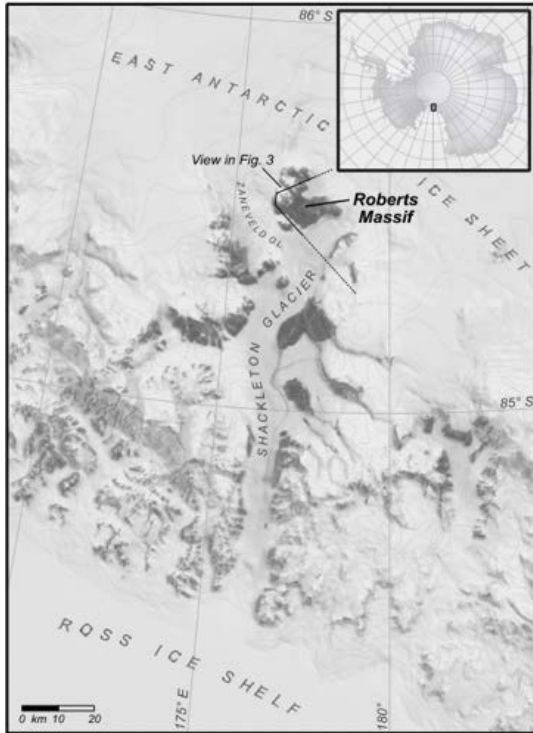


Figure 1. Location of Roberts Massif. The massif lies at the head of the Shackleton Glacier, which flows from the polar plateau of the East Antarctic Ice Sheet at ~2500 m elevation, down through the Transantarctic Mountains, to the Ross Ice Shelf near sea level. Base map generated from the MODIS MOA (Scambos et al., 2007) and Antarctic Digital Database via the Quantarctica compilation (<http://quantarctica.npolar.no>).

64 To further constrain the pre-Pleistocene configurations of the EAIS, we exploit the extensive moraine record at Roberts
 65 Massif, a high-elevation site in the central TAM, where studies on nearby nunataks have suggested that old (> 5 Ma)
 66 deposits exist (e.g., Ackert and Kurz, 2004). Roberts Massif (86.374°S, 177.135°W) is a ~100 km² ice-free area
 67 situated at the head of Shackleton Glacier, an outlet of the EAIS (Figure 1). The massif is bounded to the south and
 68 east by the EAIS, to the north and west by the upper Shackleton Glacier, and to the northeast by an unnamed branch
 69 of Zaneveld Glacier. Today, the EAIS at Roberts Massif is cold based and the environment is that of a polar desert.
 70 We employed cosmogenic ³He, ²¹Ne, ¹⁰Be, and ²⁶Al to date moraines at Roberts Massif to create a comprehensive
 71 glacial-geologic record for this site comprising 168 samples. Our record affords an unprecedented view of EAIS
 72 variability in the central TAM over the last ~15 Ma and provides valuable new insight into EAIS behavior during
 73 periods of the Miocene and Pliocene, when temperatures and atmospheric CO₂ were likely similar to or higher than
 74 today.

Deleted: 180

76 **2 Methods**

77 **2.1 Geomorphic Mapping and Sample Collection**

78 Fieldwork took place during the 2015–2016 and 2016–2017 austral summers. In the field, we identified and mapped
79 moraines, till deposits, and fault scarps on to 2 m-resolution satellite imagery provided by the Polar Geospatial Center,
80 University of Minnesota. We collected samples for surface-exposure dating from the upper surfaces of erratic boulders
81 located on moraine crests and drift sheets, focusing on boulders in stable positions (i.e., perched atop other boulders,
82 not broken) and exhibiting minimal evidence for surficial erosion. Owing to the prevalence of nuclide inheritance
83 documented by previous Antarctic cosmogenic studies (e.g., Stone et al., 2003; Todd et al., 2010), which is linked to
84 incomplete erosion by cold-based ice of previously exposed surfaces, we sampled large (generally > 1 m tall), angular
85 boulders, following the reasoning that such forms are (i) less likely to have been reworked from the underlying Sirius
86 Group tills than visibly molded, striated, and/or polished cobbles of exotic lithologies, and (ii) more likely to have at
87 least one side that is free of inherited nuclides.

88 We collected samples of ~1–5 cm thickness using either a hammer and chisel or drill and wedges. To characterize
89 each sampled boulder fully and document its geomorphic context, we described, measured, sketched, and
90 photographed each boulder from at least four different angles. We located samples in the field using an uncorrected
91 handheld GPS unit (estimated horizontal precision typically ± 6 m), and measured elevations by barometric traverse
92 from temporary benchmarks established using differentially corrected GPS and corrected to orthometric heights
93 relative to the EGM96 geoid. The estimated vertical precision of the temporary benchmarks is between ± 0.05 and \pm
94 0.3 m. For barometric differential elevation measurements relative to the benchmarks, we used a Kestrel 4000
95 barometric altimeter and looped between samples and benchmarks to correct for time-dependent changes in
96 atmospheric pressure. The estimated total uncertainty in sample elevations measured using this procedure is ± 2.5 m,
97 reflecting the precision of the DGPS surveys and the barometer, and the reproducibility of differential barometric
98 elevation measurements of representative sites also surveyed by differential GPS in this and other studies. We
99 measured topographic shielding at sample sites using handheld compass and inclinometer and the procedure described
100 by Balco et al. (2008, with accompanying online material).

101 **2.2 Cosmogenic-nuclide measurements**

102 **2.2.1 Cosmogenic helium-3 analyses**

103 We measured cosmogenic ^3He concentrations in pyroxene separated from samples of Ferrar dolerite. To separate
104 pyroxenes at the University of Maine Cosmogenic Isotope Laboratory, we followed a modified version of the method
105 described by Bromley et al. (2014). We sieved crushed samples to isolate the 125–250 μm grain size fraction, which
106 was boiled for two hours in 10% HNO_3 to remove Fe oxides and other weathering products. We then removed lighter
107 minerals (mostly plagioclase) using a water-based heavy liquid with density 2.94 g/cm^3 , and leached remaining
108 material in 5% HF to dissolve adhering plagioclase and remove outer surfaces of pyroxene grains potentially enriched
109 in implanted ^4He from U and Th decay (Blard and Farley, 2008; Bromley et al., 2014). Finally, etched pyroxenes were

110 passed through a magnetic separator and hand-picked to remove remaining contaminants under a binocular
111 microscope.

112 We then measured ^3He concentrations in clean pyroxene separates at the Berkeley Geochronology Center using the
113 BGC “Ohio” system, which consists of a MAP 215-50 sector field mass spectrometer with updated detectors and
114 counting electronics, coupled to a fully automated gas extraction and purification system. Gas extraction on this system
115 uses a laser “microfurnace” in which ~15–40 mg aliquots of pyroxene, encapsulated in Ta packets, are heated under
116 vacuum using a 150W, 810 nm diode laser coupled to a coaxial optical pyrometer in a feedback loop allowing control
117 of the pyrometer temperature. The pyrometer is calibrated by heating a thermocouple in an identical apparatus.
118 However, note that precise temperature measurement is not necessary for this work. In most cases (Table S2), we
119 extracted helium in an initial 15-minute heating step at 1225°C, followed by a second 15-minute heating step at
120 1325°C to ensure complete extraction. The second heating step typically contained 1–5% of total He released. We
121 added additional heating steps for a few representative samples to test for complete extraction, and found He signals
122 indistinguishable from blank. Gases released into the extraction line were purified by reaction with SAES getters and
123 frozen to activated charcoal at 12 K, after which helium was released into the mass spectrometer at 33 K. In all cases,
124 we measured ^4He signals on a Faraday cup and ^3He on a continuous dynode electron multiplier operated in pulse-
125 counting mode.

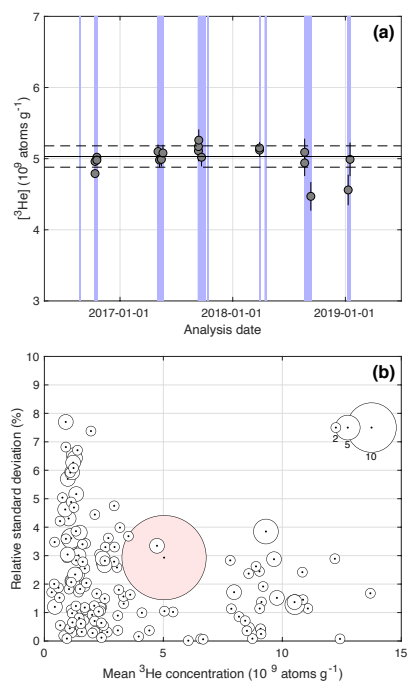


Figure 2. Quality-control data for ^3He measurements. **a)** Replicate analyses of CRONUS-P in all measurement periods during 2016-19. **Blue** lines indicate dates samples in this study were analyzed. Error bars show 68% confidence estimates (*i.e.*, 1 sigma); relatively large uncertainties and poor reproducibility in final two measurement periods reflect unusually nonlinear helium sensitivity and relatively large scatter in analyses of gas standards during these periods. Horizontal lines show mean and standard deviation of all measurements. **b)** relative standard deviation of replicate analyses of 142 samples of Ferrar pyroxene analyzed during this study. 21 of these samples are not from Roberts Massif and therefore are not reported in this study but are included here for completeness. The size of the symbol indicates the number of times each sample was analyzed. The pink circle is CRONUS-P.

Deleted: Left panel,

Deleted: r

Deleted: Light gray

Deleted: e.g.

Deleted: Right panel,

126 We quantified both ^3He and ^4He sensitivity by peak height comparison between samples and aliquots of custom-mixed
127 helium gas standards, calibrated using direct pressure measurements of both isotopes using Baratron capacitance
128 manometers, containing between 1.57×10^{-18} and 4.71×10^{-16} moles of ^3He and between 4.39×10^{-14} and 1.26×10^{-11}
129 moles of ^4He . Ferrar pyroxene has relatively high and highly variable ^4He concentrations, and the MAP 215 mass
130 spectrometer displays a significant pressure dependence on He sensitivity (Burnard and Farley, 2000), so accurately
131 quantifying machine sensitivity over a wide pressure range was an important aspect of this work. We addressed this
132 by (i) source tuning at He pressures similar to those expected for sample analyses to improve linearity in the pressure
133 range of interest, and (ii) ensuring that observed He pressures in sample analyses were bracketed within the pressure
134 range available from standard analyses. In many cases, this required discarding results of an initial analysis and
135 reanalyzing the sample with a different size aliquot calculated to match sample and standard pressures. Total process
136 blanks measured on empty Ta packets had less than 10^5 atoms ^3He and 10^{10} atoms ^4He , which is negligible for all
137 samples discussed here. Reported measurement uncertainties in ^3He concentrations include uncertainties from ^3He
138 counting statistics (typically 1–2%) as well as the variance in sensitivity inferred from gas standard analyses spanning
139 the pressure range of interest (typically 1–3%).

140 As additional quality control measures, we analyzed aliquots of the CRONUS-P pyroxene standard (Blard et al., 2015)
141 together with samples throughout each period of analysis, and made replicate analyses of a total of 121 pyroxene
142 samples as well as an additional 21 samples of Ferrar pyroxene from other Antarctic sites (Figure 2). In each of 6
143 distinct measurement periods between 2016–2019, we analyzed 2–4 aliquots of CRONUS-P. Although average
144 measured ^3He concentrations in individual measurement periods varied from $4.80 \pm 0.30 \times 10^9$ atoms/g to 5.14 ± 0.1
145 $\times 10^9$ atoms/g, data from different measurement periods were not distinguishable as separate populations. The mean
146 and standard deviation of 19 measurements during the entire period was $5.03 \pm 0.15 \times 10^9$ atoms/g (2.9%), which is
147 indistinguishable from the accepted value of 5.02×10^9 (Blard et al., 2015). Replicate analyses of other samples had
148 a mean relative standard deviation of 2.2% (Figure 2). As expected from counting statistics, replicate scatter varied
149 with ^3He concentrations, ranging from 3% for concentrations $< 2 \times 10^9$ atoms/g to 1.5% for concentrations $> 7 \times 10^9$
150 atoms/g.

151 Ferrar pyroxene is known to contain a non-zero concentration of non-cosmogenic (presumably magmatic) ^3He . Kaplan
152 et al. (2017), Margerison et al. (2005), and Ackert (2000) obtained maximum limiting concentrations for non-
153 cosmogenic ^3He of 5.7×10^6 atoms/g, which are consistent with an unpublished estimate (Balco, unpublished data)
154 of $3.3 \pm 1.0 \times 10^6$ atoms/g. As this is 1.2% of the lowest total ^3He concentration measured in a Roberts Massif erratic
155 in this study, and 0.1 % of the average concentration observed, we disregard it and assume that all observed ^3He in
156 pyroxene is cosmogenic.

157 2.2.2 Cosmogenic beryllium-10 and aluminum-26 analyses

158 We purified quartz from sandstone samples using established physical and chemical procedures (e.g., Schaefer et al.,
159 2009) at the University of Maine Cosmogenic Isotope Laboratory. Chemical extraction of beryllium and aluminum
160 and preparation of BeO and Al_2O_3 targets took place at the University of Maine and Lawrence Livermore National

Deleted:

Deleted: -

163 Laboratory (LLNL). Ratios of $^{10}\text{Be}/^9\text{Be}$ were measured relative to the 07KNSTD standard (Nishiizumi et al., 2007) at
164 LLNL and corrected for background ^{10}Be by procedural blanks with a range of 23,000–44,000 atoms. Al isotope ratios
165 are measured relative to the KNSTD standardization of (Nishiizumi, 2004), and corrected for a procedural blank of
166 $75,000 \pm 75,000$ atoms. Note that blank corrections for both ^{10}Be and ^{26}Al are negligible for samples in this study.
167 One measurement of the CRONUS-A quartz standard (Jull et al., 2015) run together with these samples yielded 3.491
168 $\pm 0.047 \times 10^7$ atoms/g ^{10}Be and $1.494 \pm 0.030 \times 10^8$ atoms/g ^{26}Al (Table S5), indistinguishable from accepted values
169 for both nuclides. Reported uncertainties for ^{10}Be and ^{26}Al measurements include uncertainties in AMS isotope ratio
170 measurement, process blanks, and $^9\text{Be}/^{27}\text{Al}$ concentrations.

171 2.2.3 Cosmogenic neon-21 analyses

172 We measured ^{21}Ne in the same quartz separates used for ^{10}Be analysis using the BGC “Ohio” noble gas mass
173 spectrometer system also used for ^3He measurements and described above. Aliquots of quartz samples were degassed
174 in two heating steps at 850° and 1100°C , and calculations of excess ^{21}Ne (see below) are based on total Ne released
175 in both heating steps. Ne isotope measurements at BGC use a ^{39}Ar spike to quantify and correct for the $^{40}\text{Ar}^{++}$
176 interference on mass 20, and are described in Balco and Shuster (2009). We quantified Ne abundances by peak height
177 comparison between samples and aliquots of an air standard containing between 5×10^{-16} and 2×10^{-14} mol Ne and
178 calibrated using a Baratron capacitance manometer. In contrast to helium, neon sensitivity was linear within this range
179 at all times. Corrections for mass discrimination, when necessary, are also based on the air standard and assumed
180 atmospheric $^{21}\text{Ne}/^{20}\text{Ne}$ and $^{22}\text{Ne}/^{20}\text{Ne}$ ratios of 0.002959 and 0.1020, respectively. A total of 20 analyses of the
181 CRONUS-A quartz standard during the period of this study yielded mean and standard deviation of 319.8 ± 6.3
182 Matoms/g (2% RSD) excess ^{21}Ne , indistinguishable from the accepted value of 320 Matoms/g (Vermeesch et al.,
183 2015).

184 Neon isotope ratios, as observed in previous studies for TAM sandstones, were indistinguishable from the
185 atmospheric-cosmogenic mixing line (see supplementary Table S3). However, Balco et al. (2019) and Middleton et
186 al. (2012) have also shown that significant concentrations of nucleogenic ^{21}Ne produced by decay of trace U and Th
187 are present in quartz from this lithology. To calculate cosmogenic ^{21}Ne concentrations in quartz samples, therefore,
188 we first calculated excess ^{21}Ne with respect to atmospheric composition, followed Balco et al. (2019) in assuming that
189 excess ^{21}Ne consists of both cosmogenic and nucleogenic ^{21}Ne , and estimated nucleogenic ^{21}Ne concentrations using
190 the following procedure. First, we measured excess ^{21}Ne concentrations in a set of six sandstone samples from ice-
191 proximal sites at upper Roberts Massif that have apparent ^{10}Be exposure ages less than 10 ka, and one additional
192 sample with an apparent ^{10}Be exposure age of 75 ka. Assuming that these samples have experienced a single period
193 of exposure, we calculated the ^{21}Ne concentration attributable to this exposure and subtracted it from total excess ^{21}Ne
194 concentrations to obtain estimates of nucleogenic ^{21}Ne ; resulting mean and standard deviation for nucleogenic ^{21}Ne
195 estimates in these samples are 10.5 ± 2.8 Matoms/g, similar to but slightly higher than estimates for Beacon Group
196 sandstones in the Dry Valleys region (Balco et al., 2019; Middleton et al. 2012). We then measured U and Th
197 concentrations in quartz and computed apparent (U-Th)/ ^{21}Ne closure ages as described in Balco et al. (2019);
198 excluding one outlier attributed to a spurious Th measurement, the mean and standard deviation of apparent closure

199 ages is 603 ± 110 Ma. If we assume that all other sandstone erratics from Roberts Massif that we analyzed in this
200 study have a similar source and therefore a similar apparent closure age, we can estimate nucleogenic ^{21}Ne
201 concentrations using U and Th concentrations and this closure age estimate. Note that this apparent closure age is
202 older than the depositional age of the Beacon Group. If these sandstone samples are derived from the Beacon group,
203 therefore, it is most likely inaccurate as a cooling age. However, the provenance of the sandstone erratics is unknown,
204 and in any case this inaccuracy would not affect the assumption that Roberts Massif sandstone erratics have a single
205 characteristic apparent closure age. Table S4 shows the results of this procedure. For samples with less than 200
206 Matoms/g total excess ^{21}Ne , we measured U and Th concentrations in individual samples and applied the mean closure
207 age inferred from the ice-proximal samples, which resulted in subtraction of up to 20% of total excess ^{21}Ne as
208 nucleogenic and had a significant effect on results. For samples with higher ^{21}Ne concentrations, the uncertainty in
209 the nucleogenic ^{21}Ne estimate is negligible and we used an average value rather than measuring U and Th in individual
210 samples. For example, for samples from the Southwest Col on Misery Platform, discussed below, estimated
211 nucleogenic ^{21}Ne is less than 0.5% of total excess ^{21}Ne . Reported uncertainties for ^{21}Ne measurements, as for ^3He , are
212 derived from counting statistics as well as reproducibility of the gas standards.

213 **2.2.4 Treatment of replicates for cosmogenic noble gas measurements**

214 For the majority of samples, we made replicate ^3He and ^{21}Ne measurements and performed chi-squared tests on
215 replicate sets with the null hypothesis that all measurements on the same sample belong to a single population and
216 disagree only because of measurement uncertainty. If we could not reject the null hypothesis at 95% confidence, we
217 took the error-weighted mean of replicate analyses as the true nuclide concentration and the standard error as the
218 uncertainty. If the null hypothesis was rejected, we used the arithmetic mean and standard deviation. A caveat to this
219 procedure, however, is that we found that our ^3He results from CRONUS-P during the period of this study did not
220 pass a chi-squared test ($p = 0.02$), indicating that our internal uncertainty estimates for individual ^3He measurements
221 are underestimating the true scatter in multiple measurements of the same sample. Thus, we adjusted calculated
222 uncertainties upward when necessary such that no ^3He concentration has a relative uncertainty less than 2.9%, the
223 relative standard deviation of CRONUS-P measurements. ^{21}Ne results from CRONUS-A, on the other hand, passed
224 the chi-squared test ($p = 0.35$), so we did not make a similar adjustment to ^{21}Ne data. However, cosmogenic ^{21}Ne
225 concentrations do include an additional uncertainty derived from nucleogenic ^{21}Ne subtraction after averaging of
226 replicates.

227 **2.3 Surface exposure age calculations**

228 We calculated exposure ages from measured nuclide concentrations using Version 3 of the online exposure age
229 calculator described by Balco et al. (2008) and subsequently updated (<http://hess.ess.washington.edu>). We employed
230 the time-dependent “LSDn” scaling method of Lifton et al. (2014) and the Antarctic atmosphere model of Stone
231 (2000). Production rate calibration for ^{10}Be , ^{26}Al , and ^3He use the “primary” calibration data sets of Borchers et al.
232 (2016) for these nuclides, and we compute ^{21}Ne production rates by assuming a $^{21}\text{Ne}/^{10}\text{Be}$ production ratio of 4.03
233 (Balco et al., 2019; Balco and Shuster, 2009b; Kober et al., 2011). In contrast to exposure-dating studies that are

234 located at similar altitude and latitude to production rate calibration sites, our study involves significant extrapolations
 235 from the locations of calibration data, mostly at low elevation and high latitude or high elevation and low latitude, to
 236 the high-elevation-high-latitude sites at Roberts Massif. Scaling methods that can be fit equivalently to the calibration
 237 data predict different production rates at our sites. Specifically, production rates predicted by LSDn scaling are ~15%
 238 higher than those predicted by the scaling method of Lal (1991) and Stone (2000) (the 'St' and 'Lm' scaling methods
 239 of Balco et al., 2008). However, at several high-elevation sites in Antarctica, including Roberts Massif, measured ^{10}Be
 240 and ^{26}Al concentrations are significantly higher than values for production-decay saturation predicted by the St and
 241 Lm methods, indicating that these methods overpredict production rates at high-elevation-high-latitude locations (see
 242 discussion in <https://cosmognosis.wordpress.com/2016/09/09/saturated-surfaces-in-antarctica/>). On the other hand,
 243 saturation concentrations predicted by the LSDn method are consistent with the highest measured ^{10}Be and ^{26}Al
 244 concentrations in Antarctica. Thus, we conclude that, at least in the high TAM, exposure ages calculated using LSDn
 245 scaling are likely accurate, and exposure ages calculated using St/Lm scaling would be spuriously old.

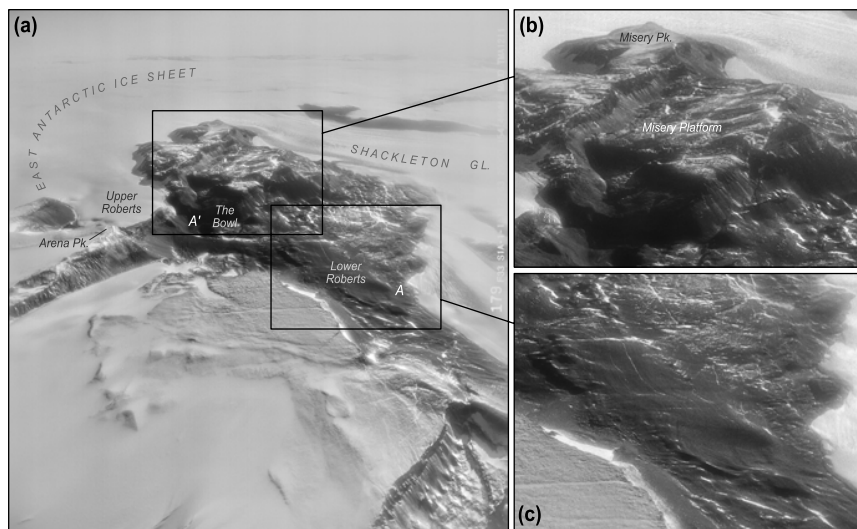


Figure 3. (a) Oblique aerial photograph of Roberts Massif looking west along the spine of the Transantarctic Mountains, with the East Antarctic Ice Sheet to the left. Enlargement (b) shows Misery Platform, which is the hanging wall of the large normal fault that bisects the massif. (c) shows the extensive moraine sequence at lower Roberts Massif. The moraine sequence at Upper Roberts (Fig. 7) faces west and is hidden from this viewing angle. The locations A and A' match Figure 4. Image is 1963 U.S. Navy trimetrogon aerial photograph, TMA 1211/179 R.

Deleted: A

Deleted: B

246 Additional uncertainties in exposure-age estimates derive from the choice of production rate calibration data.
 247 Estimated total uncertainties for ^{10}Be exposure ages derived from calibration data are ~6% (Borchers et al., 2016).
 248 Yet, any ^{10}Be calibration dataset that predicted significantly lower production rates, and therefore lower saturation
 249 concentrations, would not be consistent with the ^{10}Be data from the Southwest Col (see discussion in section 4.3).
 250 These data permit that we have underestimated ^{10}Be production rates, but not that we have overestimated them.

253 However, the majority of data in this study are ^3He exposure ages, and we have no similar constraint on ^3He production
254 rates. ^3He production rate calibration data display substantially more scatter than ^{10}Be , and estimates on total global
255 uncertainty for ^3He exposure dating range from less than 2% (Goehring et al., 2018) to more than 10% (Borchers et
256 al., 2016; Phillips et al., 2016). Production rate calibration uncertainty therefore may be significant for ^3He results.

257 **3 Results**

258 **3.1 Field Observations**

259 Roberts Massif is defined topographically by large-scale normal faulting that has produced escarpments as much as
260 ~1200 m in relief (Figure 3). These faults delineate a number of broad, sub-horizontal surfaces, including a lower-
261 elevation platform (hereafter ‘Lower Roberts’), a middle-elevation platform, comprising the Misery Platform and
262 Upper Roberts sites, and the high peaks of the massif, including Misery Peak (2725 m) and Arena Peak (informal
263 name; 2700 m). Local bedrock comprises sandstones of the Beacon Supergroup and pyroxene-bearing Ferrar dolerite,
264 which includes a fine-grained variety and a friable, coarse-grained variety. Notably, the termini of the EAIS,
265 Shackleton Glacier, and the unnamed spur of Zaneveld Glacier at Roberts Massif are relatively free of debris,
266 containing only the occasional boulder. Further, we did not observe any evidence of glacial outwash or liquid water
267 at any of these margins, indicating that the ice bounding Roberts Massif is currently cold-based.

268 **3.1.1 Lower Roberts**

269 In the southern portion of the Lower Roberts area, a complex of faults forms a deep, back-tilted basin named “The
270 Bowl” by Hambrey et al. (2003). With the exception of a 100 m-relief bedrock hill, referred to here as the Central
271 Rise, and the Bowl, the Lower Roberts area exhibits relatively gentle topography (Figure 4). Dolerite bedrock surfaces
272 outcrop at several locations throughout Roberts Massif, and commonly exhibit glacial polish, striations, and molding
273 consistent with erosion beneath a wet-based glacier. Most of these bedrock outcrops are directly overlain by semi-
274 lithified, poorly sorted pockets of sediment (several meters thick in places), containing deeply striated gravel- to
275 cobble-sized clasts of heterogenous, non-native lithologies embedded in an olive-gray, clay-rich matrix (Figures 4 and
276 5). We interpret these sediments as lodgement tills associated with the Sirius Group. First described by Mercer (1972),
277 the Sirius Group occurs throughout the upper (>~1500 m elevation) TAM as erosional remnants of clay-rich diamicton
278 that are correlated with at least one period of past temperate glaciation. An in-depth sedimentological study of glacially
279 eroded bedrock surfaces and Sirius Group tills at Roberts Massif, and other locations along upper Shackleton Glacier,
280 is provided by Hambrey et al. (2003).

281 Bedrock and Sirius Group tills are blanketed by patchy glacial drift, comprising primarily angular, cobble-to-boulder-
282 sized clasts with little-to-no fine-grained material (Figure 5). Ferrar dolerite is the most abundant lithology, although
283 this drift includes the occasional sandstone boulder, as well as rounded cobbles reworked from the underlying tills
284 described above. A key feature of this drift deposit is the abundance of open-work boulder moraines, which we
285 targeted for surface-exposure dating (Figure 6). These low relief (1–2 m high) ridges are composed primarily of large,
286 angular dolerite boulders and are oriented sub-parallel to the modern ice edge, marking former marginal positions of

Deleted: 20

288 the EAIS to the South and the unnamed spur of the Zaneveld glacier to the north. The sediments of these drifts and
 289 associated boulder-belt moraines exhibit characteristics typical of cold-based glaciation, being thin, patchy, and clast-
 290 supported with little-to-no fine-grained material (Figures 5 and 6) (Atkins, 2013). Furthermore, clasts are generally
 291 angular and lack the striations, polish, and molding associated with erosive wet-based ice.

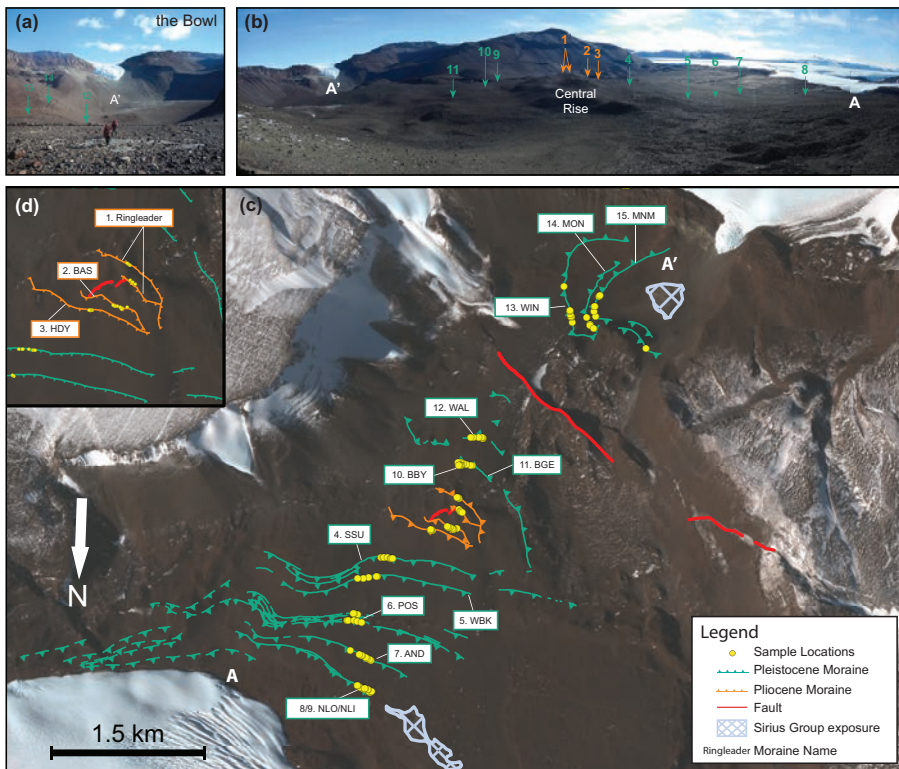


Figure 4: Map of Lower Roberts. a) Photograph of the Bowl, showing cold-based drift and moraines overlying Sirius Group deposits, which appear light gray, and b) photo of the Lower Roberts area. In (a) and (b), arrows point to sampled moraines, with numbers corresponding to moraine names in (c) and (d), and letters A and A' corresponding to positions in (c). c) Glacial geomorphic map showing moraines and sample locations at Lower Roberts, as well as the location of observed Sirius Group outcrops. The NLO/NLI and POS are moraine complexes that comprise two or more crests, and the BBY moraine is a short moraine segment just north of the BGE moraine. d) Closer view of the Pliocene-aged moraines encircling the Central Rise, shown in orange in (c). The base map is derived from Worldview-2 satellite imagery (copyright 2017, DigitalGlobe, Inc.).

292 We identified and sampled for surface-exposure dating 15 moraines throughout the Lower Roberts area. We focused
 293 on the most prominent, laterally continuous moraines, which comprise accumulations of stacked boulders, and avoided
 294 the numerous discontinuous moraine mounds and isolated erratic boulders, from which former ice marginal positions

Deleted:

Formatted: Normal, Centered

Deleted:

Deleted: shown with

Deleted: ed

299 are difficult to reconstruct. The stratigraphically oldest moraine in the Lower Roberts sequence, the Ringleader
300 moraine (informal name) encircles the summit of the Central Rise, indicating that north- and south-flowing ice masses
301 once converged to form a continuous ice surface across the Lower Roberts area at least ~170 m higher than the modern
302 ice margin to the north. From the Ringleader moraine, at the highest position in the Lower Roberts site, we sampled
303 northern (extending from Ringleader to A in Figure 4) and southern (extending from Ringleader to A' in Figure 4)
304 moraine transects. Listed in stratigraphic order, the northern transect included the BAS, HDY, SSU, WBK, POS,
305 AND, and NLO/NLI moraines (moraine initials correspond to informal names and sample ID suffixes listed in the
306 ICE-D Antarctica online database and Table S1); from the southern transect we sampled the BBY, BGE, WAL, WIN,
307 MON, and MNM moraines. Notably, the POS moraines constitute a complex of three main ridges, while the NLO/NLI
308 moraines comprise two distinct ridges spaced only by ~5 m.

309 The youngest deposit at Roberts Massif comprises a thin layer of sandstone and dolerite debris that extends several
310 tens of meters beyond the current ice margins. Clasts are relatively unweathered (i.e., exhibit minimal staining and/or
311 exfoliation), and exhibit fresh scuff marks [abrasions formed as cold-based ice drags entrained boulders across
312 underlying surfaces (Atkins et al., 2002)] (Figure 5f). With the exception of a few discontinuous segments, this unit
313 generally is not associated with distinct moraines. Based on strong similarities in position, morphology, and relative
314 weathering with deposits reported from other TAM sites (e.g., Todd et al., 2010), we correlate the youngest drift unit
315 at Roberts Massif with the most recent Late Quaternary expansion of Shackleton Glacier/EAIS and do not discuss it
316 further.

317 Outboard of this relatively unweathered limit, drift and moraine boulders become progressively more weathered with
318 distance from and elevation above the modern ice. For instance, dolerite boulders belonging to the outermost deposits
319 of the HDY, BAS, and Ringleader moraines (up to 3 km from and 170 m above the modern ice margin) exhibit dark
320 red staining, pitting of up to ~0.5 cm depth, exfoliation up to ~4 mm, and weathering rinds 1–2 mm thick, while the
321 presence of sandstone clasts is increasingly rare (Figure 6d). In contrast, dolerite boulders that we sampled on the
322 innermost moraines were generally blue-grey in color and lacked significant weathering characteristics, such as
323 staining or pitting (Figure 6c). Although the boulders on the outermost moraines at Roberts Massif display more
324 pronounced weathering than those on the inner moraines, the characteristics described here represent relatively
325 minimal surface weathering compared to slightly warmer and wetter Antarctic locations, such as the McMurdo Dry
326 Valleys. There, ~3 Ma clasts, which are similar in age to those on the HDY, BAS, and Ringleader moraines (Section
327 3.4), display pitting greater than 4 cm depth (Swanger et al., 2011). Additionally, we did not observe any cross-cutting
328 relationships between moraine crests throughout Lower Roberts, either on the ground or in satellite imagery.
329 Therefore, we conclude that moraines at this site increase in age with distance away from and elevation above the
330 modern ice sheet surface. Altogether, these surface-most deposits indicate that the Lower Roberts area records > 15
331 prior expansions of cold-based ice.



Figure 5: Views of drifts and tills described at Roberts Massif. a) The gray, fine-grained Sirius Group deposits atop striated dolerite bedrock; b) Sirius Group exposed in section in the Bowl, [with 120 cm long pole for scale](#); c) Striated, glacially molded Sirius cobble embedded in a fine-grained matrix; d) Sample 16-ROB-089-COL, a freshly-scoured sandstone clast in the Bowl, likely deposited as a thin drift sheet atop older deposits during a Late Quaternary expansion of the EAIS; e) cold-based AND moraine, which is Pleistocene in age; and f) Misery B moraine, which is Miocene in age.



Figure 6: Photographs of moraines and sampled boulders at Roberts Massif. a) Blue-gray dolerite boulder 16-ROB-010-NLO on the second moraine from the modern EAIS in the Lower Roberts northern transect; b) Red-stained dolerite boulder 16-ROB-059-RIN on the Ringleader moraine, the outermost moraine in the Lower Roberts area; c) Relatively unweathered sandstone boulder 16-ROB-009-NLO; d) Red-stained/varnished sandstone boulder 16-ROB-062-RIN on the Ringleader moraine; e) Relatively unweathered, blue-gray dolerite boulder 15-ROB-064-MUS on the Musik moraine, the innermost moraine at Upper Roberts; and f) Weathered/red-stained dolerite boulder 15-ROB-038-ARM on the Arena moraine, the outermost moraine at Upper Roberts.

Formatted Table

Deleted: ¶

Deleted: ¶

335 **3.1.2 Upper Roberts**

336 The Upper Roberts site is situated on a steep, west-facing slope of Arena Peak, directly adjacent to the northward
337 flowing lobe of the EAIS that ultimately flows over the Bowl headwall (Figure 7). Here, we mapped glacial drift and
338 moraines identical in character to those at Lower Roberts, indicating deposition by a cold-based EAIS. Similar to
339 observations at Lower Roberts, a fresh-looking drift of sandstone and dolerite boulders extends several tens of meters
340 beyond the modern ice edge. At the Upper Roberts site, that fresh deposit is associated with a low-relief (~1.5 m)
341 ridge. We attribute this deposit to the most recent expansion of the EAIS during the Late Quaternary and do not discuss
342 it further in this paper. We focused on five moraine ridges located along a vertical transect between ~60 m and 150 m
343 above and oriented sub-parallel to the modern ice surface (2150 m). In order of descending elevation, we identified
344 and sampled the Arena (2300 m), Eine (2260 m), Kleine (2240 m), Nacht (2220 m), and Musik (2220 m) moraines
345 (informal names). Additionally, we mapped moraine segments preserved both within and above (up to ~2500 m
346 elevation) this transect, but, owing to lateral discontinuity and poor preservation on high-gradient slopes, we did not
347 sample these limits for surface-exposure dating. As at Lower Roberts, the general increase in boulder-surface
348 weathering (Figure 6) and the absence of cross-cutting moraine stratigraphy (determined from field observations and
349 satellite imagery; Figure 7) suggests that glacial deposits at Upper Roberts become older with increasing elevation
350 above the modern EAIS.

Deleted: (Figure 6)

351 **3.1.3 Misery Platform**

352 Misery Platform is a broad, gently sloping platform in the southwest part of Roberts Massif (Figures 3 and 8).
353 Comprising the top surface of the hanging-wall block of a large normal fault, Misery Platform is bounded to the south
354 by a ~300–340 m-high fault scarp. At the base of the scarp, we mapped a series of arcuate moraine ridges (here termed
355 the Misery moraines), four of which we sampled for exposure-age dating (Figures 8 and 9). The southern edge of the
356 footwall block, which includes Misery Peak (2723 m elevation), drops steeply to the EAIS surface at ~2200 m
357 elevation, and exhibits south-facing, amphitheater-shaped valleys that are occupied partially by north-flowing lobes
358 of the EAIS (Figure 8). The largest of these valleys is located directly south of the Misery Moraines, and its extension
359 above the current surface of the EAIS suggests that this lobe of ice was significantly thicker in the past. Further, a thin
360 drift of glacial erratics atop the footwall block at ~2550 m elevation mark where a north-flowing lobe of the EAIS
361 overtopped the broad slopes east of Misery Peak and cascaded down the escarpment, where it deposited the Misery
362 moraines on the platform below. This interpretation requires that the Misery moraines (a) postdate the formation of
363 the fault scarp and (b) were deposited by an EAIS that was sufficiently thick (> 300 m above the current surface) to
364 overtop the footwall block. Although the Misery moraines are similar in elevation to those sampled at Upper Roberts,
365 they represent the highest former ice surface elevation of the EAIS examined in this study.

Deleted: ,

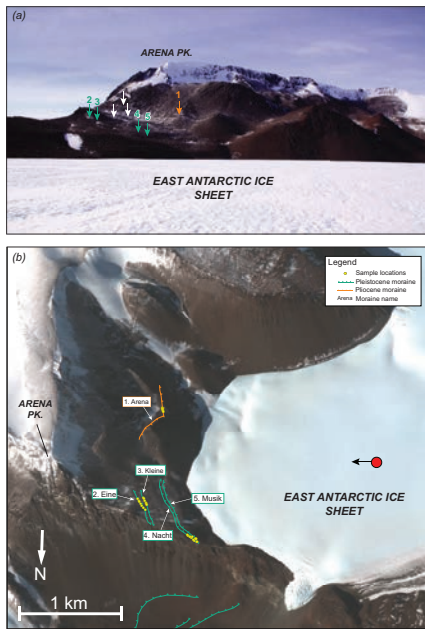


Figure 7. Upper Roberts Massif. a) Photograph of the Upper Roberts transect with moraines marked by arrows, numbered corresponding to sampled moraines in (b). White arrows in (a) denote undated moraines. b) Geomorphic map of Upper Roberts. The red circle and arrow shows the location and vantage of photo in (a). The base map in (b) is derived from Worldview-2 satellite imagery (copyright 2017, DigitalGlobe, Inc.).

368 Compared to moraines at Lower and Upper Roberts, the Misery moraines are relatively broad and high-relief (~2–5
 369 m high) and comprise finer matrix material (silt-to-gravel). Moraine crests are mantled with angular dolerite boulders
 370 exhibiting pronounced weathering features, including deep red-to-purple staining, 2–3 mm-thick weathering rinds,
 371 and ventifaction pits of up to 2 cm depth. On the basis of these physical characteristics, they appear older than the
 372 outermost moraines at both Lower and Upper Roberts. Therefore, we interpret the Misery moraines as cold-based ice-
 373 marginal features marking the ostensibly oldest and most extensive EAIS terminus positions that we documented at
 374 Roberts Massif. We used cross-cutting relationships of the Misery moraines to determine their stratigraphic order.
 375 From outermost (oldest) to innermost (youngest), we sampled boulders on the following moraine crests: Misery D,
 376 Misery A, Misery B, Misery C (note that the designations A-D are field designations reflecting the sequence of sample
 377 collection, not the stratigraphic order; Figure 8). Importantly, we avoided sampling adjacent to overlapping moraine
 378 segments.

379 Immediately outside of, and stratigraphically underlying, the Misery moraines, the weathered bedrock surface is
 380 mantled with a thin patchy ablation till, dominated by dolerite boulders and a small number of sandstone clasts, and
 381 associated with a coarse-grained sand and gravel deflation surface. We observed this unit throughout Misery Platform
 382 and collected samples for surface-exposure dating from boulders on Southwest Col, located approximately 1.5 km
 383 northwest of the Misery moraine complex and 400 m above the modern surface of Shackleton Glacier (Figure 8).
 384 Here, the ablation till ('Southwest Col drift') mantles a bedrock surface of heavily stained and deeply exfoliated

385 coarse-grained dolerite. In places, granular sediments fill joints and depressions in the bedrock. These sediments are
386 characterized by red-stained silt-to-gravel-sized grains, which may derive from the disintegration of the dolerite
387 bedrock, and gravel-to-cobble-sized clasts of various lithologies. In contrast to the Sirius Group deposits observed
388 elsewhere at Roberts Massif, boulders comprising Southwest Col drift are predominantly dolerite (as opposed to a
389 broad mix) and generally more angular.

390 We sampled three dolerite clasts (1 boulder and 2 cobbles) and four sandstone clasts (3 boulders and 1 cobble), all of
391 which are perched on bedrock and/or interstitial sediments, for surface-exposure dating. The surface of the dolerite
392 boulder (15-ROB-28-COL) exhibits deep red staining and evidence of significant wind abrasion, except on the lee
393 side where there is a thick red-brown weathering rind (Figure 9). The sandstone boulders (15-ROB-32-COL, 15-ROB-
394 33-COL, and 15-ROB-34-COL) exhibit orange-to-red staining, surface varnish, and ventifaction of up to 4 cm depth.
395 Based on the thin nature of this deposit, we interpret the Southwest Col drift as a cold-based ablation till deposited by
396 the EAIS. Owing to its weathering state, we suggest that this deposit is the oldest glacial unit in our record. Surface-
397 exposure ages from this site therefore provide a minimum-limiting age for temperate glaciation at Roberts Massif.

398 **3.1.4 Summary of Field Observations**

399 We mapped three primary surfaces at Roberts Massif (listed in stratigraphic order): glacially molded and striated
400 dolerite bedrock, temperate-style tills belonging to the Sirius Group, and cold-based drifts associated with openwork
401 boulder moraines. All samples collected for surface-exposure dating are derived from the cold-based deposits marking
402 former positions of the EAIS. At both the Lower and Upper Roberts sites, weathering patterns and the lack of cross-
403 cutting moraines suggest that relative moraine ages increase with distance from, and elevation above, the modern ice
404 sheet margin. Deposits on Misery Platform (the Misery moraines and the Southwest Col drift) exhibit more advanced
405 subaerial weathering than our other sites, indicating that these deposits are significantly older. In Section 4.2, we
406 describe results from cosmogenic-nuclide measurements made on samples from 23 separate moraine ridges and one
407 drift sheet.

Deleted: 3

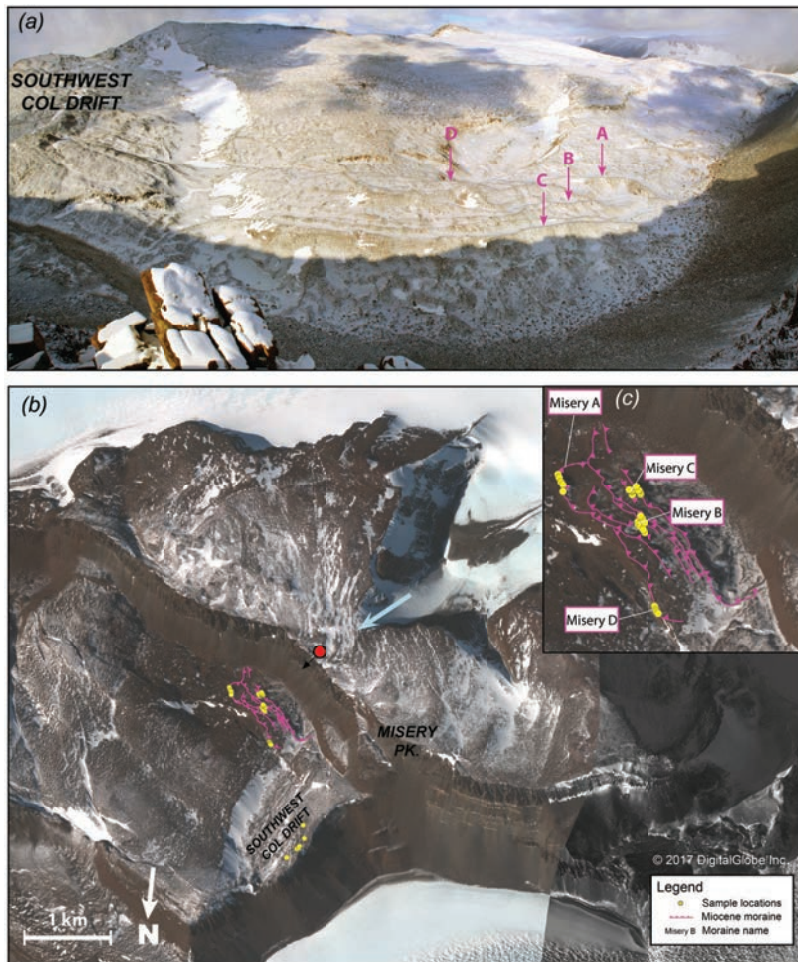


Figure 8: Map of Misery Platform. a) Photo of the Misery Moraines. Pink arrows point to the sampled Misery Moraines and are labelled with the corresponding moraine letter. The location of the Southwest Col Drift is also labeled. The photo was taken from the location of the red circle in (b) looking in the direction of the black arrow (vantage to the northeast). b) Geomorphic map of the Southwest Col area. The Southwest Col Drift mantles the bedrock outboard of the Misery moraines. The blue arrow denotes the direction of ice flow when the Misery Moraines were deposited. [\(c\) Closer view of the Misery moraine complex.](#) The base map in (b) and (c) is derived from Worldview-2 satellite imagery (copyright 2017, DigitalGlobe, Inc.).

Deleted: drift



Figure 9: Photographs of boulders from the Misery Platform. a) Dolerite boulder 15-ROB-017-MZC on the Misery C moraine; b) Dolerite boulder 15-ROB-028-COL at the Southwest Col; c) Sandstone boulder 15-ROB-035-COL at the Southwest Col; d) Sandstone cobble 15-ROB-029-COL at the Southwest Col.

410 3.2 Results from Cosmogenic-Nuclide Measurements

411 We made 293 cosmogenic ^3He measurements in pyroxene from 155 dolerite boulders; 32 ^{21}Ne and 13 ^{10}Be
 412 measurements in quartz from 13 sandstone boulders; and two ^{26}Al measurements in quartz from two sandstone
 413 boulders (also measured for ^{21}Ne and ^{10}Be). Samples were derived from 23 distinct moraine crests and one glacial
 414 drift sheet (Southwest Col). Apparent exposure ages span two periods: ~13–8 Ma at Misery Platform and ~3 Ma–400
 415 ka at Upper and Lower Roberts (Tables 1 and S1). “Apparent” exposure ages refer to the calculated age of the boulder
 416 given the measured nuclide inventory, assuming that the boulder has experienced only one period of exposure, with
 417 no erosion or burial during that time. Boulder information, nuclide concentrations, complete step-degassing results for
 418 ^3He and ^{21}Ne are summarized in Tables S2, S3, and S5, and the full dataset is archived online in the ICE-
 419 D:ANTARCTICA database (<http://antarctica.ice-d.org>). In this section, we summarize these cosmogenic-nuclide data



Deleted:

Deleted: 67

Deleted: 8

Deleted: 3

424 and highlight the possible effects of surface erosion and other geomorphic processes on exposure ages, which
425 ultimately lead us to estimates of the emplacement age of the moraines.

426 **3.2.2 Constraints on erosion rates from paired ^{10}Be - ^{21}Ne measurements**

427 As the majority of landforms at Roberts Massif are several million years old, quantifying the magnitude of surface
428 erosion is key to accurate exposure-dating. Here, we summarize geochemical data and field observations that allow
429 us to place limits on long-term erosion rates. Four sandstone erratics at Southwest Col have ^{10}Be concentrations close
430 to predicted production-erosion saturation values, and apparent ^{21}Ne exposure ages of 9–12 Ma. As these samples
431 have nearly the highest concentrations of these nuclides yet measured on Earth, concentration measurements are
432 correspondingly (and unusually) precise, making it possible to use the paired $^{10}\text{Be}/^{21}\text{Ne}$ data to simultaneously infer
433 exposure ages and surface erosion rates from these samples (Figure 10) (Gillespie and Bierman, 1995; Lal, 1991).
434 Given the assumption that these samples have experienced continuous exposure at a steady erosion rate, the $^{10}\text{Be}/^{21}\text{Ne}$
435 data imply true exposure ages in the range 12–15 Ma, but varying surface erosion rates in the range 0.5–3 cm/Myr.
436 These low erosion rates are consistent with our field observations pertaining to surface erosion of these sandstones as
437 described in Section 3.1.3.

438 Apparent ^3He exposure ages from three dolerite clasts also located on Southwest Col, and which therefore should have
439 the same true exposure age as the sandstone clasts, are 8.6 Ma, 10 Ma, and 11 Ma. Assuming that the true exposure
440 age of the deposit is no greater than 14.5 Ma, as implied by the two-nuclide data for the highest-nuclide-concentration
441 sandstone (15-ROB-032-COL) shown in Figure 10, this implies maximum erosion rates for the dolerite clasts of 3.8,
442 2.7, and 1.9 cm/Myr, respectively. Further assuming that the dolerite clast with the highest ^3He concentration (15-
443 ROB-028-COL) has been exposed at the drift surface for the longest period, and has therefore experienced mainly
444 surface weathering rather than exhumation from till, we propose that ~2 cm/Myr is likely a maximum limit on rock
445 surface erosion rates for dolerite surfaces in our study area. The assumption that this clast has been exposed at the
446 surface is supported by the fact that 15-ROB-028-COL is a boulder, while the rest of the dolerite surfaces we sampled
447 on Southwest Col are cobbles. If the deposit is younger than 14.5 Ma, an even lower erosion rate would be implied.
448 Although this is an extremely low surface weathering rate by global standards, it is nonetheless consistent with the
449 polar desert climate and the field observations described in section 3.1.3 (i.e., angular clasts with surface varnish and
450 minimal pitting).

451 **3.2.3 Information about geomorphic processes from multiple-nuclide measurements**

452 As on Southwest Col, we also measured multiple nuclides (^{10}Be and ^{21}Ne , and, in one case, ^{26}Al) in several sandstone
453 boulders on the Ringleader, WIN, MON, AND, and NLO moraines at Lower Roberts (Figure 11). Although sandstone
454 clasts are rare on these moraines, these data provide some insight into the exposure history of these boulders that we
455 can use to assess the importance of inheritance and post-depositional disturbance for moraine exposure ages.

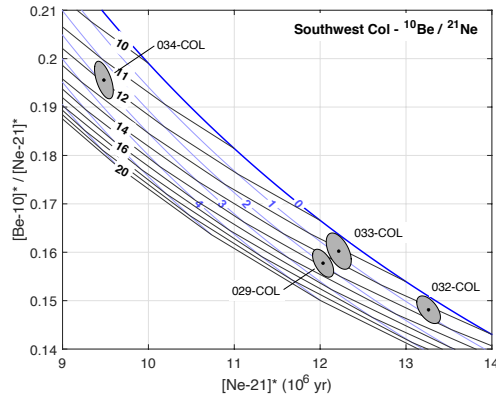
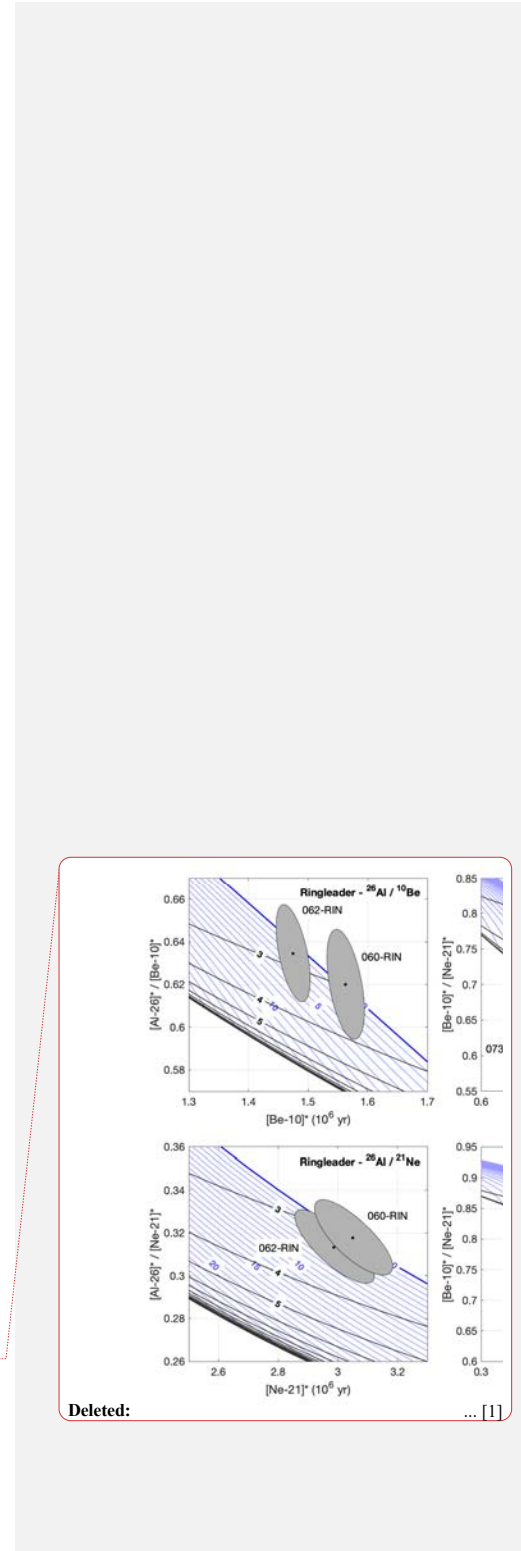


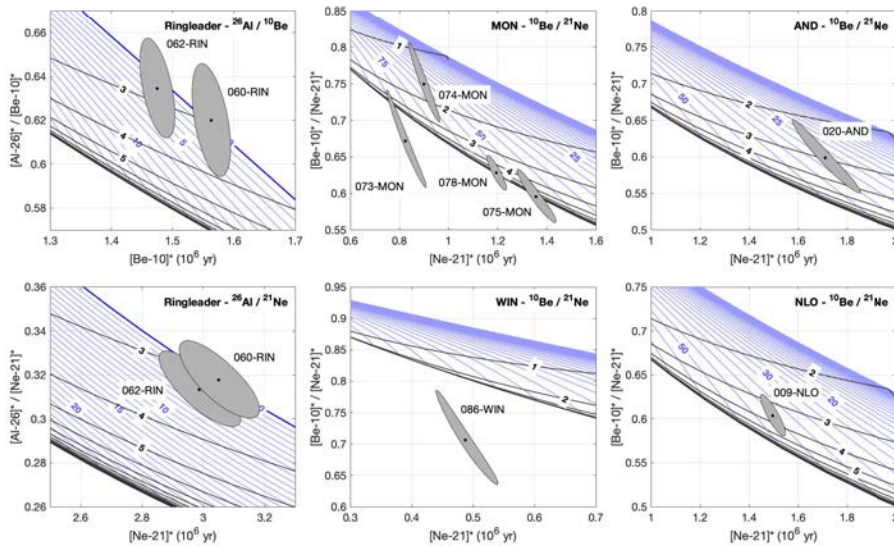
Figure 10. ^{10}Be - ^{21}Ne normalized two-nuclide diagram for Southwest Col sandstone erratics. Blue lines are isolines of constant steady erosion (cm/Myr); black lines are isolines of constant exposure age (Ma). The diagram is constructed using LSDn production rate scaling and a $^{21}\text{Ne}/^{10}\text{Be}$ production ratio of 4.03 (Balco et al., 2019). Note that the x-coordinate, the ^{21}Ne concentration normalized to the production rate, is equivalent to the apparent ^{21}Ne exposure age. Although apparent ^{21}Ne exposure ages for these samples are 9.5–13 Ma, the two-nuclide diagram shows that the data are better explained by 12–15 Ma exposure at erosion rates between 0.5–3 cm/Myr.

456 In general, a boulder that has experienced a single period of exposure that is equal to the emplacement age of the
 457 moraine should display concordant ^{10}Be , ^{21}Ne , and ^{26}Al ages that are the same as those of other boulders on the
 458 moraine. For the Ringleader moraine (Figure 11), ^{10}Be - ^{21}Ne - ^{26}Al measurements are concordant at 2.8–3 Ma, therefore
 459 consistent with simple exposure at negligible erosion, and lie in the center of the range of ^3He ages from dolerite clasts
 460 on the same moraine (Figure 12). These observations suggest that (i) the sandstone boulders have experienced a single
 461 period of exposure with minimal post-depositional exhumation or weathering, which is consistent with our field
 462 observations as described in section 3.1.1, (ii) their exposure age most likely represents the true emplacement age of
 463 the moraine, and (iii) two outliers in the ^3He age distribution can likely be attributed to both inheritance (one ~4 Ma
 464 age) and post-depositional disturbance (one ~2 Ma age) .

465 In contrast, paired ^{10}Be - ^{21}Ne measurements on four boulders on the MON moraine and one on the WIN moraine
 466 (Figure 11), both adjacent to the Bowl and emplaced by ice from upper Roberts overflowing the Bowl headwall (Figure
 467 4), display discordant apparent ages. Additionally, apparent exposure ages from both sandstone and dolerite boulders
 468 at these moraines are relatively scattered (coefficient of variance > 20%). The ^{10}Be - ^{21}Ne data (Figure 11) could be
 469 explained either (i) by an extended period of steady erosion at an ice-free site prior to entrainment and deposition of
 470 the clasts, or (ii) by repeated exposure and ice cover of the samples prior to emplacement. Both of these conditions
 471 are likely if these boulders were sourced from the adjacent outcrop area of sandstone on the Bowl headwall (Figure
 472 4a). Thus, we consider it most plausible that the apparent exposure ages of these sandstones reflect prior exposure
 473 and, thus, overestimate the true age of the moraine. In general, these results imply that high scatter in exposure ages



Deleted: ... [1]



475

476 **Figure 11.** Two-nuclide diagrams for all sandstone erratics collected from lower Roberts Massif moraines. The
 477 construction of the diagrams is the same as in Fig. 10. Two-nuclide data for sandstones on the Ringleader moraine lie
 478 on the simple exposure line and are in agreement with ^3He ages, suggesting that these samples experienced a single
 479 period of exposure at negligible erosion, and their apparent ages are a good estimate of the true age of the moraine.
 480 On the other hand, paired nuclide data from sandstones on the MON, WIN, AND, and NLO moraines require either
 481 significant erosion or a multistage exposure history. An erosion explanation would predict that their apparent ages
 482 should be younger than ^3He ages on the same moraines; as this is not the case, these samples most likely experienced
 483 a multistage exposure history and therefore were emplaced with significant nuclide inheritance.

484 for moraines in the Bowl are most likely explained by inherited nuclide concentrations in clasts sourced from the
 485 adjacent headwall, and the true ages of the moraines are therefore likely close to the young end of their age
 486 distributions.

487 Finally, paired ^{10}Be - ^{21}Ne measurements from the AND and NLO moraines (Figure 11), both at the ice-proximal end
 488 of the northern Lower Roberts transect, fall within the “erosion island” on the two-nuclide diagram, indicating that
 489 their true exposure ages are older than the apparent ages for either nuclide. In addition, these clasts have apparent ages
 490 higher than most ^3He ages from these moraines (Figure 12). Again, this is best explained if the scatter exhibited by
 491 these moraines is largely the result of inheritance.

492 Overall, although we have a relatively small number of multiple-nuclide data from sandstone boulders, our results
 493 demonstrate that (i) inheritance is unequivocally present in some moraine boulders and (ii) inheritance is likely most
 494 significant at moraines where boulders are likely sourced from a combination of far-traveled EAIS subglacial debris

Formatted: Font: Bold

495 and cliff fall within the massif itself. These scenarios are also consistent with the observation that boulders on moraines
496 at upper Roberts, which can only be derived from beneath the EAIS, exhibit substantially less scatter than moraines
497 at lower Roberts (Table 1 and Figure 12), where additional input from rockfall is likely. Overall, while none of our
498 observations exclude post-depositional disturbance as a potential source of scatter, they do show that inheritance is
499 likely a more important contributor. However, the small number of young outliers in our dataset (Figure 12) may
500 reflect the ablation of an ice core from the moraine.

501 3.3 Outlier Elimination

502 For each moraine dated, we measured cosmogenic nuclides in 6–8 individual clasts. We observed a variety of
503 distributions ranging from tightly grouped age sets, which likely reflect dispersion due to measurement uncertainties
504 alone, to highly scattered distributions with both old (indicative of nuclide inheritance) and young outliers (e.g., due
505 to ablation of an ice core from the moraine, subaerial weathering and/or post-depositional disturbance, such as rock
506 toppling or cracking). To interpret these age distributions and arrive at realistic estimates of the moraine age, we
507 utilized constraints from field observations, the stratigraphic ordering of the moraines, exposure-age trends across
508 moraine transects, and measurements of multiple nuclides in various clasts (see above).

509 We first considered geomorphic stratigraphy, weathering characteristics, and trends in exposure-age distributions to
510 identify and eliminate outliers. For Misery Platform, we utilized the cross-cutting relationships of the Misery moraines,
511 which elucidate relative age, to identify exposure ages that are outliers. Although we did not observe such cross-
512 cutting relationships at Upper and Lower Roberts, we exploited the fact that both apparent exposure ages and physical
513 weathering state increase with distance from and elevation above the modern ice margins to determine relative ages
514 of the moraines, and thus to identify likely outliers.

515 We performed an initial screening to remove outliers by assuming that the true depositional age of each moraine lies
516 within the range of measured exposure ages on this moraine. If true, then any exposure ages on one moraine that are
517 older than all exposure ages on a stratigraphically older moraine must be erroneous. Likewise, any exposure ages that
518 are younger than all ages on a stratigraphically younger moraine must also be erroneous. Applying this rule recursively
519 to stratigraphically ordered sets of moraines resulted in the rejection of 46 measurements on 22 boulders (Figures 12
520 and 13; Table S1). We also rejected 9 measurements on 5 boulders as outliers likely resulting from geomorphic
521 processes (i.e., inheritance or post-depositional disturbance), which were not rejected as stratigraphic outliers yet are
522 $> 2\sigma$ beyond the main age population on that moraine (see Table S1). After this stratigraphic screening was complete,
523 we also rejected as outliers 14 non-concordant ^{10}Be and ^{21}Ne measurements on 10 sandstone boulders located on the
524 NOLO, AND, WIN, and MON moraines, as those boulders likely contain inherited nuclides (see discussion in Section
525 3.2.3). In total, we rejected 69 measurements on 37 boulders (Figures 12 and 13; Table S1).

526 The resulting boulder age distributions for each moraine exhibit a variety of forms. Many moraines (e.g., Arena, BAS,
527 Misery B moraines; Figures 12 and 13) display a central cluster approximating a normal distribution, and for these
528 moraines we assign the mean and standard deviation of the ages as the best estimate of the depositional age of the
529 moraine. Other moraines (e.g., SSU, WAL, BGE) showed heavily skewed, bimodal, or scattered age distributions; for

Deleted: ---

531 these we provide age ranges rather than means in the discussion that follows. In the case of those high-scatter moraines,
532 it is likely that the true moraine age is closer to the younger end of the age range, as we identified inheritance as a
533 more likely contributor to moraine scatter than post-depositional disturbance (Section 3.2.3).

534 3.4 Moraine ages

535 In this section, we summarize moraine age estimates assuming zero surface erosion (Table 1; Figures 12 and 13); we
536 discuss the effects of this assumption in later sections.

537 **Lower Roberts:** The oldest dated moraine in the Lower Roberts area – Ringleader – dates to 2.94 ± 0.24 Ma. Along
538 a northward transect from the summit of the Central Rise to the modern ice margin, subsequent moraines yielded the
539 following ages (moraine initials correspond to informal names and sample ID suffixes listed in the ICE-D Antarctica
540 online database; Figure 12): BAS (2.94 ± 0.14 Ma), HDY (2.84 ± 0.08 Ma), WBK ($1.62\text{--}2.84$ Ma), SSU ($1.90\text{--}2.95$
541 Ma), POS ($1.16\text{--}2.05$ Ma), AND ($1.08\text{--}1.63$ Ma), NLO ($1.07\text{--}1.58$ Ma), NLI ($0.54\text{--}2.09$ Ma). A similar transect
542 extending southward from the Central Rise provides the following moraine ages: BBY ($1.55\text{--}2.69$ Ma), BGE (1.41--
543 2.93 Ma), WAL ($1.50\text{--}2.80$ Ma), WIN ($0.51\text{--}1.00$ Ma), MON (0.54 ± 0.01 Ma), and MNM ($0.40\text{--}0.87$ Ma). As
544 discussed in section 3.2.3, this southern transect displays the highest degree of age scatter, potentially due to the
545 incorporation of rockfall from the surrounding escarpments.

546 **Upper Roberts:** Moraine ages at Upper Roberts display a high degree of internal consistency and are reported here
547 from highest moraine to lowest: Arena (2.64 ± 0.13 Ma); Eine (1.19 ± 0.14 Ma); Kleine (1.18 ± 0.16 Ma); Nacht (1.11
548 ± 0.10); and Musik ($0.61\text{--}1.10$ Ma) (Figure 12). As noted in section 4.1, undated moraine segments located above the
549 Arena moraine represent higher surface levels of the EAIS, potentially prior to ~ 2.6 Ma. Additionally, undated
550 moraine segments situated between the Arena and Eine moraines, which differ in elevation by ~ 45 m, may account
551 for the temporal gap between these two limits.

552 **Misery Moraines:** Approximately 1.5 km southeast of the Southwest Col drift (~ 14.5 Ma, section 3.2.2), the Misery
553 moraines yielded ages (listed from outermost moraine to innermost) of 7.94 ± 0.23 Ma (Misery D; $n = 4$), 7.93 ± 0.23
554 Ma (Misery A; $n = 1$), 7.99 ± 0.06 Ma (Misery B; $n = 8$), and 7.63 ± 0.29 Ma (Misery C; $n = 5$) (Figure 13). We
555 consider a young population of ages, between ~ 4 and 6 Ma, on the Misery A and Misery C moraines to be outliers as
556 the bulk of ages from the complex cluster around 8 Ma. Due to the excellent internal consistency of these age
557 populations, we consider it unlikely that the 8 Ma population reflects inheritance, as that mechanism typically
558 introduces considerable scatter to the data set (Balco, 2011).

Deleted: 1

Deleted: S

Deleted: 4.2.4

Deleted: 1

Deleted: S

Deleted: 2

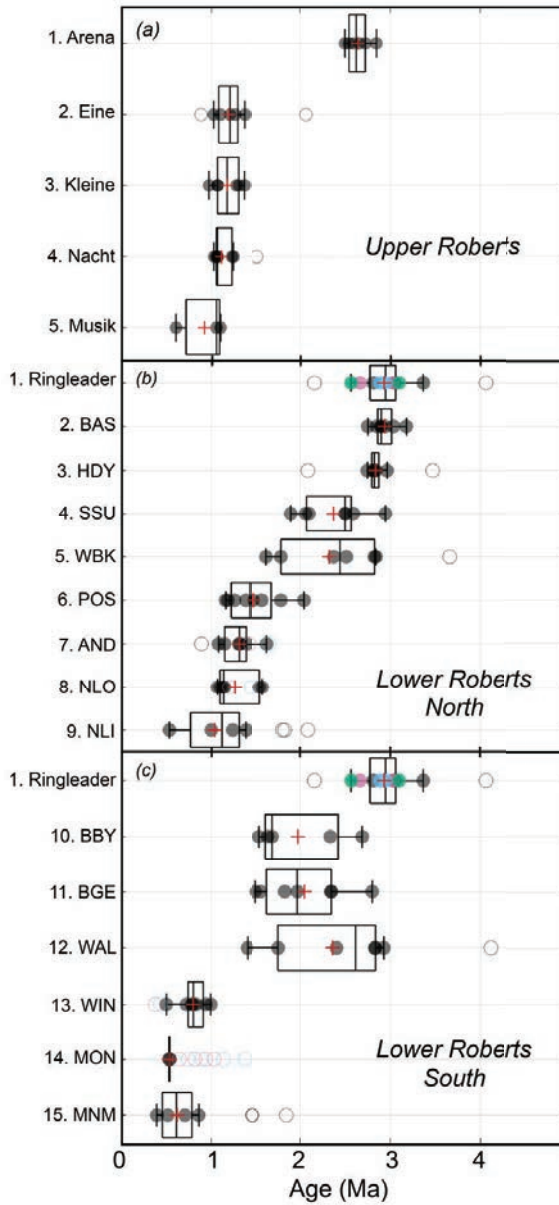


Figure 12: Boxplots showing moraine ages for the Plio-Pleistocene part of the Roberts Massif record. Moraines for each site (Upper Roberts and Lower Roberts northern and southern transects) are listed in stratigraphic order, with the outermost moraine at the top of each panel. Moraine numbers in (a) correspond to those in Figure 7, while moraine numbers in (b) and (c) correspond to those in Figure 4. The Ringleader moraine is shown in both panels (b) and (c), as it is the uppermost moraine in both Lower Roberts transects. ^3He ages are black, ^{21}Ne ages are blue, ^{10}Be ages are pink, and ^{26}Al ages are green. Outliers are shown as open circles. The average moraine age is denoted by a red plus symbol.

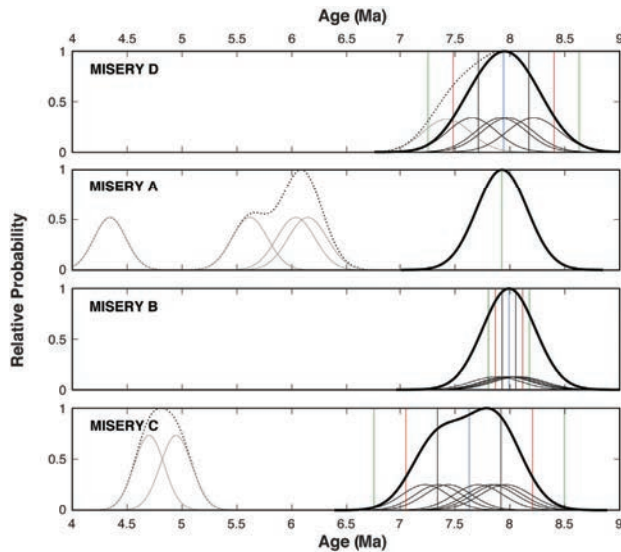


Figure 13: Camel plots (i.e., normal kernel density functions) for the four Misery moraines. The arithmetic mean of the reduced dataset is denoted by the blue line, while the 1σ , 2σ , and 3σ uncertainty envelopes are shown in black, red, and green, respectively. Dotted black lines show the summed probability distributions for the full dataset, including outliers shown in gray, while the thick black lines show the probability distribution for the reduced dataset.

565 **4 Discussion**

566 Cosmogenic-exposure ages on moraines and glacial drift at Roberts Massif afford unprecedented insight into Late
 567 Cenozoic variability of the EAIS. The record begins at ~14.5 Ma (Southwest Col drift), while distinct ice-marginal
 568 positions date to ~8 Ma and between ~3–1 Ma. As described in Section 3.1, all moraines are characteristic of cold-
 569 based glacial conditions and are oriented sub-parallel to the modern EAIS margins, suggesting ice configuration
 570 similar to today at high elevation in the central TAM. Recognizing the influence of Ross Sea ice on even the uppermost
 571 reaches of transverse EAIS outlet glaciers (Mercer, 1968; Bockheim et al., 1989; Denton et al., 1989; Orombelli et al.,
 572 1990; Denton and Hall, 2000; Bromley et al., 2010, 2012), we speculate that the Roberts Massif moraines formed
 573 when Ross Sea ice (either an ice shelf or grounded ice sheet) buttressed Shackleton Glacier and thus that ice
 574 configuration in the Ross Sea Embayment was similar to today for considerable parts of our record. In the following
 575 sections, we discuss the length of the Roberts Massif glacial-geologic record and address the climatic implications of
 576 our findings.

Formatted: Justified, Space Before: 6 pt, Line spacing: 1.5 lines

Deleted: 4

578 **4.1 Uplift at Roberts Massif**

579 Relative to previous glacial-geologic archives from Antarctica, the Roberts Massif record is exceptionally long (~14.5
580 Ma). At all three sites described in [section 3.1](#), moraine age increases with distance from and elevation above the
581 modern EAIS, with the oldest site (Misery Platform) ostensibly indicating the thickest ice. One hypothesis to explain
582 the age-elevation relationship at Roberts Massif is that, while the massif itself has remained isostatically stable for
583 duration of our record, the surface elevation of the EAIS during glacial maxima has lowered systematically over time.
584 Alternatively, the configuration of the EAIS during glacial maxima has remained roughly constant for the duration of
585 the record, but the underlying bedrock has undergone uplift due to tectonism, dynamic topography, and/or isostasy,
586 processes relevant to the millions-of-years timescale. Tectonic uplift at Roberts Massif since ~15 Ma likely was
587 minimal; apatite fission thermochronology in the central TAM suggests that major faulting due to tectonism was
588 complete by ~30 Ma (Fitzgerald, 1994; Miller et al., 2010). However, over the last 3 Myr, approximately 40 m of
589 uplift at Roberts Massif may be attributed to dynamic topography (Austermann et al., 2015), though this value cannot
590 account fully for the ~3 Ma ice positions situated ~170 m (Ringleader moraines) and ~180 m (Arena moraine) higher
591 than the modern EAIS at Lower and Upper Roberts, respectively.

592 Instead, isostatic rebound resulting from deepening of outlet glacier troughs (i.e., removal of rock and replacement by
593 less dense ice) may account for much of the apparent moraine elevation loss through the Roberts Massif record. While
594 large portions of EAIS outlet glaciers, including Shackleton Glacier, are likely frozen to the bed, and thus minimally
595 erosive, regions of these glaciers are thick enough to be at the pressure melting point today (Golledge et al., 2014),
596 and thus eroding their beds ([Bader et al., 2016](#); [Graly et al., 2018](#)). Removal of several hundred meters of rock since
597 the mid-Miocene would therefore result in isostatic rebound of a few hundred meters ([Van der Wateren et al., 1999](#);
598 [Stern and Tenbrink, 1989](#)). Although we cannot quantify total trough erosion over the course of our record, this
599 magnitude of uplift is consistent with the observed elevational offset between relict moraines and the modern EAIS.

600 As well as elucidating deposition age, near-saturation concentrations of ^{10}Be on Southwest Col (15-ROB-033-COL)
601 and ^{26}Al the Ringleader moraine (16-ROB-062-RIN) afford maximum-limiting values for isostatic uplift at Roberts
602 Massif, both since ~14.5 Ma and during the last 3 Myr. For these samples, ^{10}Be and ^{26}Al concentrations become
603 saturated (with respect to LSDn scaling) with erosion rates of $\sim 2.3 \text{ g cm}^{-2} \text{ Myr}^{-1}$ and $\sim 7 \text{ g cm}^{-2} \text{ Myr}^{-1}$, respectively. If
604 we assume that this apparent erosion rate reflects not removal of mass by surface weathering, but rather a decrease in
605 atmospheric depth due to uplift, these erosion rate values provide maximum uplift rates. The ^{10}Be saturation erosion
606 rate for 15-ROB-033-COL yields an uplift rate of $\sim 24 \text{ m Myr}^{-1}$ over the last ~14 Myr, indicating that the total
607 maximum uplift over the course of the record is ~350 m, or ~70 m over the last 3 Myr. This estimate accounts for less
608 than half of the elevation difference between the ~3 Ma Ringleader moraine and the EAIS margin (~170 m). In
609 contrast, the ^{26}Al saturation erosion rate for 16-ROB-062-RIN affords a higher uplift rate of $\sim 70 \text{ m Myr}^{-1}$ over the last
610 3 Myr, or ~210 m over the Plio-Pleistocene portion of the record, a value that accounts for the full ~170 m elevation
611 difference between the Ringleader moraine and the modern EAIS. Importantly, both the 24 m Myr^{-1} and 70 m Myr^{-1}
612 values each represent maximum uplift rates under the assumption of zero erosion, meaning that the average pace of
613 uplift during the Plio-Pleistocene may not have differed from that during the last ~14.5 Ma. In fact, because ^{26}Al does

Deleted: and the buttressing presence of grounded ice in the Ross Sea Embayment (e.g., Alonso et al., 1992; Bromley et al., 2010; Hauptvogel and Passchier, 2012). In the following sections, we discuss the length of the Roberts Massif glacial-geologic record and address the climatic implications of our findings. ¶

Deleted: S

Deleted: 4

622 not quite reach saturation in 3 Myr, it is likely that the 70 m Myr⁻¹ is an overestimate. Moreover, the true uplift rate at
623 Roberts Massif probably was lower than those calculated here, since our field observations indicated that some, albeit
624 minor, post-depositional surficial erosion has taken place (Section 3.1).

625 Uplift of $\leq \sim 200$ m over the Plio-Pleistocene is consistent with cosmogenic-nuclide concentrations from the McMurdo
626 Dry Valleys, which indicate minimal vertical change during this period (Brook et al., 1995). Similarly, ⁴⁰Ar/³⁹Ar ages
627 on subaerial volcanic cones limit uplift to 300 m in the Dry Valleys over the past 3 Ma (Wilch et al., 1993) and < 67
628 m in the Royal Society Range over the past 7.8 Ma (Sugden et al., 1999). In contrast, Stern et al. (2005) posit that > 1
629 km of isostatic uplift throughout the central TAM has occurred since 35 Ma due to glacial erosion. If true, the
630 cosmogenic-nuclide concentrations presented here imply that nearly all of this uplift must have taken place between
631 35 and 14 Ma.

632 Given the likelihood of isostatic uplift over the long duration of our record, which potentially accounts for much of
633 the offset between moraine elevations and the modern EAIS, we cannot evaluate changes in ice thickness throughout
634 this ~14 Myr record with certainty. However, we emphasize that a large, cold-based ice sheet with configuration
635 similar to today was present during the dated parts of this record.

636 4.2 Miocene presence of the EAIS

637 The oldest dated glacial unit at Roberts Massif, Southwest Col drift, was deposited ~14.5 Ma and demonstrates that
638 the EAIS in the central TAM was cold-based by at least the mid-Miocene (Figure 14). This finding aligns closely with
639 earlier work from the northern TAM that placed the transition to polar conditions at ~14–15 Ma (Denton and Sugden,
640 2005). We note that deposition of Southwest Col drift also coincided broadly with a mid-Miocene climatic shift
641 documented in the Olympus Range, McMurdo Dry Valleys, where well-preserved terrestrial and lacustrine fossils
642 interbedded with ash fall deposits have been interpreted as reflecting an 8°C cooling of Antarctic summers at ~14.5
643 Ma (Lewis et al., 2008). In addition, the age of Southwest Col drift, which provides a minimum-limiting age for cold-
644 based glaciation in the central TAM, is approximately coeval with the Mid-Miocene Cooling Transition (~15–13 Ma),
645 marked by a decline in global sea-surface and bottom-water temperatures (Lear et al., 2015) and atmospheric CO₂
646 concentrations (Zhang et al., 2013). Finally, Southwest Col drift affords minimum-limiting age constraint for the
647 underlying Sirius Group till at Roberts Massif and supports previously published surface-exposure data suggesting
648 that these temperate deposits are > 5 Ma (Ivy-Ochs et al., 1995; Schaefer et al., 1999).

649 Overlying Southwest Col drift, the ~8 Ma Misery moraines represent the oldest ice-marginal landforms identified at
650 Roberts Massif and suggest the presence of a large, cold-based ice sheet at that time. This EAIS configuration is
651 broadly coincident with elevated sea-surface temperatures (Herbert et al., 2016) and Antarctic Bottom Water
652 temperatures (Lear et al., 2015), and potentially higher atmospheric CO₂ (Sosdian et al., 2018) relative to the Plio-
653 Pleistocene. Therefore, our record suggests that a substantial EAIS occupied the central TAM at ~8 Ma despite
654 generally warmer-than-present climatic conditions (Figure 14).

Deleted: ≤

Deleted: -

Deleted: 3

658 **4.3 Plio-Pleistocene presence of the EAIS**

659 The majority of moraines in the Roberts Massif record date to ~3–1 Ma, thus documenting the persistence of a large
660 EAIS during the Plio-Pleistocene transition and early Pleistocene (Figure 14). Because the uncertainties in our moraine
661 ages (~0.1–0.5 Ma) exceed the 40-kyr climate cycles dominant during the pre-MPT world, we do not assign moraines
662 to individual climate events, such as Marine Isotope Stages (i.e., Lisiecki and Raymo, 2005; Railsback et al., 2015).
663 Nonetheless, moraines dated to > ~2.5 Ma indicate a large EAIS in the central TAM during times when global
664 temperatures and atmospheric CO₂ were likely higher than today (Willeit et al., 2019).

665 Several moraines at Roberts Massif date to ~3 Ma (Ringleader, ~3 Ma; BAS, ~3 Ma; HDY, ~2.8 Ma; Arena, ~2.6
666 Ma), inviting the question of whether any of these landforms correspond to the Mid-Pliocene Warm Period (MPWP:
667 ~3.3–3.0 Ma), which has garnered attention as a plausible analog for modern anthropogenic warming. The ongoing
668 debate regarding the resilience of the EAIS during the MPWP bears two leading hypotheses: (i) that the EAIS was of
669 similar extent, or potentially larger, than today during the MPWP (e.g., Sugden et al., 1993; Winnick and Caves, 2015)
670 due to increased East Antarctic precipitation under warmer atmospheric conditions (Huybrechts, 1993); and (ii) that
671 the EAIS was significantly smaller than today (Scherer et al., 2016; Webb et al., 1984) as a result of enhanced melting
672 along marine margins (Pollard and DeConto, 2016) and associated structural collapse (Pollard et al., 2015). At Roberts
673 Massif, moraines dating to the MPWP would support the first hypothesis; however, an absence of MPWP moraines
674 neither proves nor disproves the second hypothesis, as geologic evidence for even a slightly smaller EAIS would lie
675 beneath the modern ice sheet surface (Balco, 2015). Below, we address the possibility that any Roberts Massif
676 moraines date to the MPWP, given the uncertainties associated with exposure dating (i.e., erosion, production rate
677 error, and uplift).

678 First, we address the possibility that erosion of boulder surfaces, which acts to remove a portion of the cosmogenic
679 nuclide inventory, yielded erroneously young apparent exposure ages for the Late Pliocene moraines. As shown in
680 Section 3.2.3, concordant ¹⁰Be-²¹Ne-²⁶Al measurements on Ringleader sandstones afford an exposure age of ~3 Ma,
681 consistent with the ³He ages on that moraine, and both sandstone and dolerite boulders appear to have experienced
682 relatively minimal erosion (i.e., angular, minimal pitting and exfoliation; Section 3.1.1). Applying the maximum
683 surface erosion rate for dolerites of 2 cm/Myr, determined using the ³He concentration of 15-ROB-028-COL (Section
684 3.2.2), the average dolerite age on Ringleader is 3.18 Ma and thus within the uncertainty of the apparent moraine age.
685 Together, our field observations and cosmogenic-nuclide measurements suggest that the apparent age of the
686 Ringleader moraine is not erroneously young due to surface erosion. As discussed in Section 4.1, the maximum
687 possible error in moraine age due to uplift is the same as that for erosion, meaning that the inclusion of uplift has no
688 significant impact on moraine age.

689 Next, we explore the potential effect of cosmogenic nuclide production-rate uncertainty on moraine age. The ¹⁰Be
690 production rate is accompanied by ~6% error and ³He by ~10% error (Borchers et al., 2016), meaning that the
691 Ringleader moraine could be ~6 % older (with a lower production rate) or younger (with a higher production rate),
692 using the more precise ¹⁰Be production rate as a limit (note: ¹⁰Be and ³He ages are statistically indistinguishable).
693 However, we can use the boulder with the highest ¹⁰Be concentration on Southwest Col (15-ROB-033-COL), which

Deleted: 3

695 is close to saturation, to provide a lower limit for the ^{10}Be production rate. Applying a production rate $\sim 2\%$ lower than
696 the globally calibrated production rate of Borchers et al. (2016), which we used to calculate the ^{10}Be ages presented
697 here, sample 15-ROB-033-COL becomes oversaturated with respect to LSDn scaling, suggesting that, at most, the
698 Ringleader moraine (the oldest in the Plio-Pleistocene sequence) is no older than ~ 3 Ma. Conversely, if the true
699 production rate is higher than that of Borchers et al. (2016), it is possible that the Ringleader moraine is up to 6%
700 younger (~ 2.8 Ma) than reported here. As there are no sandstones on the oldest landform in the Upper Roberts
701 sequence – Arena Moraine (~ 2.7 Ma) – we assess the full 10% range in ^3He production rate. Assuming a 10% reduction
702 in production rate, the Arena moraine could date to ~ 3 Ma, or the end of the MPWP.

703 In summary, we did not date any moraines unequivocally to the MPWP, suggesting that the EAIS was not significantly
704 larger than today during that time. However, given the dataset presented here, we cannot evaluate further the
705 configuration of the EAIS during the MPWP because evidence for the ice sheet extent during that time lies beneath
706 the modern glacier. Moreover, we note that our moraine chronology lacks landforms dating to the earlier Pliocene (~ 5
707 Ma), when conditions are thought to have been as warm as during the MPWP (Burke et al., 2018). Nevertheless, our
708 current dataset provides evidence for a large, cold-based EAIS in the central TAM during the Late Pliocene,
709 immediately following the MPWP, and in the early-to-mid Pleistocene.

710 **5 Conclusions**

711 Surficial deposits characteristic of cold-based glaciation at Roberts Massif span the Last Glacial Maximum to Mid-
712 Miocene, thereby providing an exceptionally long geologic record of glaciation for the central TAM. The preservation
713 of numerous, vertically offset ice-marginal deposits is most plausibly explained by the persistence of an EAIS similar
714 in configuration to today during multiple glacial maxima, accompanied by gradual isostatic uplift of Roberts Massif.
715 Coupled with extremely low erosion rates ($\ll 5$ cm/Myr), the prevalence of cold-based deposition over the last ~ 14.5
716 Ma supports persistent polar desert climate conditions in East Antarctica since the mid-Miocene. Our record also
717 provides minimum-limiting age control for the underlying Sirius Group deposits, suggesting that at least some of the
718 temperate glacial deposits preserved in the TAM are older than 14.5 Ma.

719 Although the Roberts Massif record is not a direct measure of East Antarctic ice volume, our dataset indicates that the
720 EAIS was not any larger during the late Pliocene-early Pleistocene than it was during parts of the Miocene, even
721 though temperatures cooled progressively through the Plio-Pleistocene. Nonetheless, the absence at Roberts Massif
722 of ice-marginal deposits dating unequivocally to the MPWP highlights a critical area for continued investigation, since
723 distal paleoclimate evidence and model simulations suggest the EAIS was smaller than present at that time. Accepting
724 that geologic evidence for even a slightly smaller EAIS during the MPWP would lie beneath the modern ice sheet, we
725 cannot further evaluate the extent to which the EAIS was smaller during the MPWP with the current data set from
726 Roberts Massif.

727 In summary, the Roberts Massif dataset provides a long-term, terrestrial perspective of ice sheet extent in the central
728 TAM, and shows that the EAIS has been a persistent feature of this region since the mid-Miocene. Throughout this

729 record, the EAIS has maintained a configuration similar to today, which requires the presence of buttressing ice in the
 730 Ross Sea Embayment, and by extension, West Antarctica, even during periods when global temperature and
 731 atmospheric CO₂ concentrations likely were similar to or higher than present.

Deleted:
 Deleted: grounded

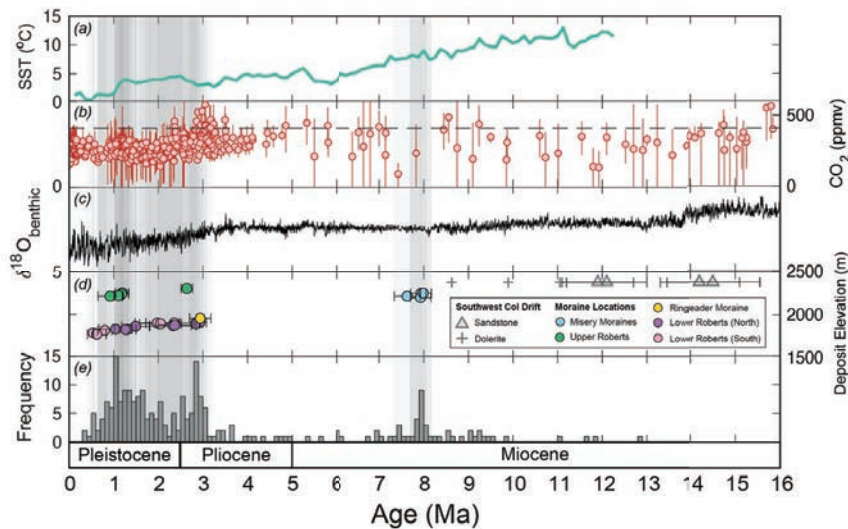


Figure 14: Comparison between Roberts Massif glacial chronology and relevant climate records. (a) Southern Hemisphere alkenone-derived temperature stack (Herbert et al., 2016); (b) Boron-isotope-, paleosol-, and stomata-derived CO₂ records (Beerling et al., 2009; Breecker and Retallack, 2014; Da et al., 2019; Dyez et al., 2018; Ji et al., 2018; Sosdian et al., 2018; Wang et al., 2015; Zhang et al., 2013) (c) benthic oxygen isotope stack (De Vleeschouwer et al., 2017), (d) Moraine age and uncertainty at Roberts Massif, plotted against deposit elevation. Note that deposition of the Misery moraines required ice to be > 300 m thicker than today, which is not reflected in the moraine elevation. The age of the Southwest Col sandstones account for erosion, as described in section 3.2.2 (e) Histogram of all apparent exposure ages at Roberts Massif, including outliers. Vertical gray bars denote moraine ages, including uncertainty. Darker gray color shows a higher frequency of moraines.

Deleted: d
 Deleted: e
 Deleted:
 Deleted: Blue circles are the Misery moraines, teal circles are Upper Roberts moraines, the yellow circle is the Ringleader moraine, purple circles are moraines in the Lower Roberts northern transect, pink circles are moraines in the Lower Roberts southern transect, gray plus signs are apparent ages of dolerite boulders of the Southwest Col Drift, and gray triangles are the age of the Southwest Col sandstones, accounting for erosion,
 Deleted: f
 Deleted: Colors on the timescale at the bottom correspond to moraine colors in Figures 4, 7, and 8.

732 **Data Availability**

733 All analytical information associated with cosmogenic-nuclide measurements appear in the supplementary tables.
 734 Analytical information, with additional sample documentation and photographs, is also available in the ICE-
 735 D:ANTARCTICA online database (<http://antarctica.ice-d.org/>).

752 **Author Contribution**

753 All authors conducted fieldwork, sample collection, and sample preparation for cosmogenic-nuclide analyses. Balco,
754 Balter and Thomas carried out cosmogenic noble gas measurements, and were responsible for data reduction and
755 analysis. Balter prepared the manuscript with contributions from Balco and Bromley.

756 **Competing Interests**

757 The authors declare that they have no conflict of interest.

758 **Acknowledgements**

759 This work was supported by U.S. National Science Foundation grants ANT-1443329 and ANT-1443321 and by the
760 Ann and Gordon Getty Foundation. It would not have been possible without major contributions from many elements
761 of the U.S. Antarctic Program, including the 109th Airlift Wing of the New York Air National Guard, pilots and
762 ground crews of Kenn Borek Air, and many USAP staff at Shackleton Glacier Camp and McMurdo Station. In
763 addition, we thank Chris Simmons for field mountaineering support, Tim Becker for assistance with noble gas
764 measurements at BGC, Kaj Overturf for help with sample crushing and sieving at the University of Maine, and Brenda
765 Hall for insightful discussions. Geospatial support for this work was provided by the Polar Geospatial Center under
766 NSF-OPP awards 1043681 and 1559691.

767 **References**

768 Ackert, R. P.: Antarctic glacial chronology : new constraints from surface exposure dating., Ph.D. thesis, Woods
769 Hole Oceanographic Institution, Massachusetts Institute of Technology, United States of America, 213 pp.,
770 2000.

771 Ackert, R. P. and Kurz, M. D.: Age and uplift rates of Sirius Group sediments in the Dominion Range, Antarctica,
772 from surface exposure dating and geomorphology, *Glob. Planet. Change*, 42, 207–225, 2004.

773 ~~Atkins, C. B.: Geomorphological evidence of cold-based glacier activity in South Victoria Land, Antarctica, *Geol.*
774 *Soc. London, Spec. Publ.*, 381(1), 299–318, doi:10.1144/SP381.18, 2013.~~

775 Atkins, C. B., Barrett, P. J. and Hicock, S. R.: Cold glaciers erode and deposit: Evidence from Allan Hills,
776 Antarctica, *Geology*, 30(7), 659–662, doi:10.1130/0091-7613(2002)030<0659:CGEADE>2.0.CO;2, 2002.

777 Austermann, J., Pollard, D., Mitrovica, J. X., Moucha, R., Forte, A. M., DeConto, R. M., Rowley, D. B. and Raymo,
778 M. E.: The impact of dynamic topography change on Antarctic ice sheet stability during the mid-Pliocene
779 warm period, *Geology*, 43(10), 927–930, doi:10.1130/G36988.1, 2015.

Deleted: Alonso, B., Anderson, J. B., Diaz, J. I. and Bartek, L. R.: Pliocene-Pleistocene Seismic Stratigraphy of the Ross Sea: Evidence for Multiple Ice Sheet Grounding Episodes, *Contrib. to Antarct. Res.* III, 57, 93–103, 1992.

Deleted: a

Deleted: i

Deleted: -p

788 [Bader, N.A., Licht, K.J., Kaplan, M.R., Kassab, C.: East Antarctic ice sheet stability recorded in a high-elevation](#)
789 [ice-cored moraine, *Quat. Sci. Rev.*, 159, 88–102, doi: <https://doi.org/10.1016/j.quascirev.2016.12.005>,](#)
790 [2017.](#)

791 Balco, G.: The absence of evidence of absence of the East Antarctic Ice Sheet, *Geology*, 43(10), 943–944,
792 doi:10.1130/focus102015.1, 2015.

793 Balco, G.: Saturated Surfaces in Antarctica: [www.cosmognosis.wordpress.com/2016/09/09/saturated-surfaces-in-](http://www.cosmognosis.wordpress.com/2016/09/09/saturated-surfaces-in-antarctica/)
794 [antarctica/](http://www.cosmognosis.wordpress.com/2016/09/09/saturated-surfaces-in-antarctica/), last access: 15 February 2020, 2016.

795 Balco, G. and Shuster, D. L.: ^{26}Al - ^{10}Be - ^{21}Ne burial dating, *Earth Planet. Sci. Lett.*, 286(3–4), 570–575,
796 doi:10.1016/j.epsl.2009.07.025, 2009a.

797 Balco, G. and Shuster, D. L.: Production rate of cosmogenic ^{21}Ne in quartz estimated from ^{10}Be , ^{26}Al , and ^{21}Ne
798 concentrations in slowly eroding Antarctic bedrock surfaces, *Earth Planet. Sci. Lett.*, 281(1–2), 48–58,
799 doi:10.1016/j.epsl.2009.02.006, 2009b.

800 Balco, G., Stone, J. O., Lifton, N. A. and Dunai, T. J.: A complete and easily accessible means of calculating surface
801 exposure ages or erosion rates from ^{10}Be and ^{26}Al measurements, *Quat. Geochronol.*, 3, 174–195,
802 doi:10.1016/j.quageo.2007.12.001, 2008.

803 Balco, G., Blard, P. H., Shuster, D. L. and Stone, J. O. H.: Cosmogenic and nucleogenic ^{21}Ne in quartz in a 28-
804 meter sandstone core from the McMurdo Dry Valleys, Antarctica, *Quat. Geochronol.*, 52, 63–76, 2019.

805 Beerling, D. J., Fox, A. and Anderson, C. W.: Quantitative uncertainty analyses of ancient atmospheric CO_2
806 estimates from fossil leaves, *Am. J. Sci.*, 309, 775–787, doi:10.2475/09.2009.01, 2009.

807 Blard, P. H. and Farley, K. A.: The influence of radiogenic ^4He on cosmogenic ^3He determinations in volcanic
808 olivine and pyroxene, *Earth Planet. Sci. Lett.*, 276, 20–29, doi:10.1016/j.epsl.2008.09.003, 2008.

809 Blard, P. H., Balco, G., Burnard, P. G., Farley, K. A., Fenton, C. R., Friedrich, R., Jull, A. J. T., Niedermann, S.,
810 Pik, R., Schaefer, J. M., Scott, E. M., Shuster, D. L., Stuart, F. M., Stute, M., Tibari, B., Winckler, G. and
811 Zimmermann, L.: An inter-laboratory comparison of cosmogenic ^3He and radiogenic ^4He in the
812 CRONUS-P pyroxene standard, *Quat. Geochronol.*, 26, 11–19, doi:10.1016/j.quageo.2014.08.004, 2015.

813 [Bockheim, J.G., Wilson, S.C., Denton, G.H., Andersen, B.G., Stuiver, M., 1989. Late Quaternary ice-surface](#)
814 [fluctuations of Hatherton Glacier, Transantarctic Mountains. *Quat. Res.*, 31, 229-254.](#)

815 Borchers, B., Marrero, S., Balco, G., Caffee, M., Goehring, B., Lifton, N., Nishiizumi, K., Phillips, F., Schaefer, J.
816 and Stone, J.: Geological calibration of spallation production rates in the CRONUS-Earth project, *Quat.*
817 *Geochronol.*, 31, 188–198, doi:10.1016/j.quageo.2015.01.009, 2016.

818 Breecker, D. O. and Retallack, G. J.: Refining the pedogenic carbonate atmospheric CO_2 proxy and application to
819 Miocene CO_2 , *Palaeogeogr. Palaeoclimatol. Palaeoecol.*, 406, 1–8, doi:10.1016/j.palaeo.2014.04.012,
820 2014.

Formatted: Superscript

Formatted: Superscript

Formatted: Superscript

821 [Bromley, G.R., Hall, B.L., Stone, J.O. and Conway, H., 2012. Late Pleistocene evolution of Scott Glacier, southern](#)
822 [Transantarctic Mountains: implications for the Antarctic contribution to deglacial sea level. *Quat. Sci. Rev.*,](#)
823 [50, 1-13.](#)

824 Bromley, G. R. M., Hall, B. L., Stone, J. O., Conway, H. and Todd, C. E.: Late Cenozoic deposits at Reedy Glacier,
825 Transantarctic Mountains: implications for former thickness of the West Antarctic Ice Sheet, *Quat. Sci.*
826 *Rev.*, 29(3-4), 384-398, doi:10.1016/j.quascirev.2009.07.001, 2010.

827 Bromley, G. R. M., Winckler, G., Schaefer, J. M., Kaplan, M. R., Licht, K. J. and Hall, B. L.: Pyroxene separation
828 by HF leaching and its impact on helium surface-exposure dating, *Quat. Geochronol.*, 23, 1-8,
829 doi:10.1016/j.quageo.2014.04.003, 2014.

830 Brook, E. J., Kurz, M. D., Ackert Jr., R. P., Denton, G. H., Brown, E. T., Raisbeck, G. M. and Yiou, F.: Chronology
831 of Taylor Glacier Advances in Arena Valley, Antarctica, Using in Situ Cosmogenic ³He and ¹⁰Be, *Quat.*
832 *Res.*, 39, 11-23, 1993.

833 Brook, E. J., Brown, E. T., Kurz, M. D., Ackert, R. P., Raisbeck, G. M. and Yiou, F.: Constraints on Age, Erosion,
834 and Uplift of Neogene Glacial Deposits in the Transantarctic-Mountains Determined From in-Situ
835 Cosmogenic Be-10 and Al-26, *Geology*, 23(12), 1063-1066, doi:10.1130/0091-7613(1995)0232.3.CO;2,
836 1995.

837 Brown, E. T., Edmond, J. M., Raisbeck, G. M., Yiou, F., Kurz, M. D. and Brook, E. J.: Examination of surface
838 exposure ages of Antarctic moraines using in situ produced ¹⁰Be and ²⁶Al, *Geochim. Cosmochim. Acta*,
839 55, 2269-2283, doi:10.1016/0016-7037(91)90103-C, 1991.

840 Bruno, A. L., Baur, H., Graf, T., Schlkhter, C., Signer, P. and Wieler, R.: Dating of Sirius Group tillites in the
841 Antarctic Dry Valleys with cosmogenic ³He and ²¹Ne, *Earth Planet. Sci. Lett.*, 147, 37-54,
842 doi:http://dx.doi.org/10.1016/S0012-821X(97)00003-4, 1997.

843 Burke, K. D., Williams, J. W., Chandler, M. A., Haywood, A. M., Lunt, D. J. and Otto-Bliesner, B. L.: Pliocene and
844 Eocene provide best analogs for near-future climates, *Proc. Natl. Acad. Sci. U. S. A.*, 115(52), 13288-
845 13293, doi:10.1073/pnas.1809600115, 2018.

846 Burnard, P. G. and Farley, K. A.: Calibration of pressure-dependent sensitivity and discrimination in Nier-type noble
847 gas ion sources, *Geochemistry, Geophys. Geosystems*, 1, doi:10.1029/2000GC000038, 2000.

848 Da, J., Zhang, Y. G., Li, G., Meng, X. and Ji, J.: Low CO₂ levels of the entire Pleistocene epoch, *Nat. Commun.*, 10,
849 1-9, doi:10.1038/s41467-019-12357-5, 2019.

850 [Denton, G.H., Bockheim, J.G., Wilson, S.C., Leide, J.E., 1989. Late Quaternary ice surface fluctuations of](#)
851 [Beardmore Glacier, Transantarctic Mountains. *Quat. Res.*31, 183-209.](#)

852 [Denton, G.H., Hall, B.L., 2000. Glacial and Paleoclimatic history of the Ross Ice drainage system of Antarctica.](#)
853 [*Geogr. Ann.*, 87 A\(1\), 139-432.](#)

854 Denton, G. H. and Sugden, D. E.: Meltwater features that suggest Miocene ice-sheet overriding of the Transantarctic
855 Mountains in Victoria Land, Antarctica, *Geogr. Ann.*, 87 A(1), 67–85, 2005.

856 Denton, G. H., Sugden, D. E., Marchant, D. R., Hall, B. L. and Thomas, I.: East Antarctic Ice Sheet Sensitivity To
857 Pliocene Climatic Change From a Dry Valleys Perspective, *Geogr. Ann.*, 75(4), 155–204, 1993.

858 Dyez, K. A., Hönisch, B. and Schmidt, G. A.: Early Pleistocene Obliquity-Scale pCO₂ Variability at ~1.5 Million
859 Years Ago, *Paleoceanogr. Paleoclimatology*, 33(11), 1270–1291, doi:10.1029/2018PA003349, 2018.

860 Fitzgerald, P. G.: Thermochronologic constraints on post-Paleozoic tectonic evolution of the central Transantarctic
861 Mountains, Antarctica, *Tectonics*, 13(4), 818–836, doi:10.1029/94TC00595, 1994.

862 Gasson, E., DeConto, R. M., Pollard, D. and Levy, R. H.: Dynamic Antarctic ice sheet during the early to mid-
863 Miocene, *Proc. Natl. Acad. Sci. U. S. A.*, 113(13), 3459–3464, doi:10.1073/pnas.1516130113, 2016.

864 Gillespie, A. R. and Bierman, P. R.: Precision of terrestrial exposure ages and erosion rates estimated from analysis
865 of cosmogenic isotopes produced in situ, *J. Geophys. Res.*, 100(B12), doi:10.1029/95jb02911, 1995.

866 Goehring, B. M., Muzikar, P. and Lifton, N. A.: Establishing a Bayesian approach to determining cosmogenic
867 nuclide reference production rates using He-3, *Earth Planet. Sci. Lett.*, 481, 91–100,
868 doi:10.1016/j.epsl.2017.10.025, 2018.

869 Gollledge, N. R., Marsh, O. J., Rack, W., Braaten, D. and Jones, R. S.: Basal conditions of two Transantarctic
870 Mountains outlet glaciers from observation-constrained diagnostic modelling, *J. Glaciol.*, 60(223), 855–
871 866, doi:10.3189/2014JoG13J131, 2014.

872 Graly, J.A., Licht, K.J., Kassab, C.M., Bird, B.W., Kaplan, M.R.: Warm-based basal sediment entrainment and far-
873 field Pleistocene origin evidenced in central Transantarctic blue ice through stable isotopes and internal
874 structures, *J. Glaciol.*, 64(244), 185-196, doi: 10.1017/jog.2018.4, 2018.

875 Herbert, T. D., Lawrence, K. T., Tzanova, A., Peterson, L. C., Caballero-Gill, R. and Kelly, C. S.: Late Miocene
876 global cooling and the rise of modern ecosystems, *Nat. Geosci.*, 9(11), 843–847, doi:10.1038/ngeo2813,
877 2016.

878 Holbourn, A., Kuhnt, W., Clemens, S., Prell, W. and Andersen, N.: Middle to late Miocene stepwise climate
879 cooling: Evidence from a high-resolution deep water isotope curve spanning 8 million years,
880 *Paleoceanography*, 28(4), 688–699, doi:10.1002/2013PA002538, 2013.

881 Huybrechts, P.: Glaciological Modelling of the Late Cenezoic East Antarctic Ice Sheet: Stability or Dynamism,
882 *Geogr. Ann.*, 75 A, 221–238, 1993.

883 Ivy-Ochs, S., Schluchter, C., Kubik, P. W., Dittrich-Hannen, B. and Beer, J.: Minimum ¹⁰Be exposure ages of early
884 Pliocene for the Table Mountain plateau and the Sirius Group at Mount Fleming, Dry Valleys, Antarctica,
885 *Geology*, 23(11), 1007–1010, doi:10.1130/0091-7613(1995)023<1007:MBEAOE>2.3.CO;2, 1995.

Deleted: ¶

Deleted: Hauptvogel, D. W. and Passchier, S.: Early-Middle Miocene (17-14Ma) Antarctic ice dynamics reconstructed from the heavy mineral provenance in the AND-2A drill core, Ross Sea, Antarctica, *Glob. Planet. Change*, 82–83, 38–50, doi:10.1016/j.gloplacha.2011.11.003, 2012....

893 Ji, S., Nie, J., Lechler, A., Huntington, K. W., Heitmann, E. O. and Breecker, D. O.: A symmetrical CO₂ peak and
894 asymmetrical climate change during the middle Miocene, *Earth Planet. Sci. Lett.*, 499, 134–144,
895 doi:10.1016/j.epsl.2018.07.011, 2018.

896 Jull, A. J. T., Scott, E. M. and Bierman, P.: The CRONUS-Earth inter-comparison for cosmogenic isotope analysis,
897 *Quat. Geochronol.*, 26, 3–10, doi:10.1016/j.quageo.2013.09.003, 2015.

898 Kaplan, M. R., Licht, K. J., Winckler, G., Schaefer, J. M., Bader, N., Mathieson, C., Roberts, M., Kassab, C. M.,
899 Schwartz, R. and Graly, J. A.: Middle to Late Pleistocene stability of the central East Antarctic Ice Sheet at
900 the head of Law Glacier, *Geology*, 45(11), 963–966, doi:10.1130/G39189.1, 2017.

901 Kober, F., Alfimov, V., Ivy-Ochs, S., Kubik, P. W. and Wieler, R.: The cosmogenic ²¹Ne production rate in quartz
902 evaluated on a large set of existing ²¹Ne-¹⁰Be data, *Earth Planet. Sci. Lett.*, 302, 163–171,
903 doi:10.1016/j.epsl.2010.12.008, 2011.

904 Lal, D.: Cosmic ray labeling of erosion surfaces: in situ nuclide production rates and erosion models, *Earth Planet.*
905 *Sci. Lett.*, 104, 424–439, 1991.

906 Lear, C. H., Coxall, H., Foster, G. L., Lunt, D. J., Mawbey, E. M., Rosenthal, Y., Sosdian, S. M., Thomas, E. and
907 Wilson, P. A.: Neogene ice volume and ocean temperatures: Insights from infaunal foraminiferal Mg/Ca
908 paleothermometry, *Paleoceanography*, 30, 1437–1454, doi:10.1002/2015PA002833. Received, 2015.

909 Levy, R., Harwood, D., Florindo, F., Sangiorgi, F., Tripathi, R., von Eynatten, H., Gasson, E., Kuhn, G., Tripathi, A.,
910 Deconto, R., Fielding, C., Field, B., Gollledge, N., McKay, R., Naish, T., Olney, M., Pollard, D., Schouten,
911 S., Talarico, F., Warny, S., Willmott, V., Acton, G., Panter, K., Paulsen, T., Taviani, M., Askin, R., Atkins,
912 C., Bassett, K., Beu, A., Blackstone, B., Browne, G., Ceregato, A., Cody, R., Cornamusini, G., Corrado, S.,
913 Del Carlo, P., Di Vincenzo, G., Dunbar, G., Falk, C., Frank, T., Giorgetti, G., Grelle, T., Gui, Z.,
914 Handwerker, D., Hannah, M., Harwood, D. M., Hauptvogel, D., Hayden, T., Henrys, S., Hoffmann, S.,
915 Iacoviello, F., Ishman, S., Jarrard, R., Johnson, K., Jovane, L., Judge, S., Kominz, M., Konfirst, M.,
916 Krissek, L., Lacy, L., Maffioli, P., Magens, D., Marciano, M. C., Millan, C., Mohr, B., Montone, P.,
917 Mukasa, S., Niessen, F., Ohneiser, C., Passchier, S., Patterson, M., Pekar, S., Pierdominici, S., Raine, I.,
918 Reed, J., Reichelt, L., Riesselman, C., Rocchi, S., Sagnotti, L., Sandroni, S., Schmitt, D., Speece, M.,
919 Storey, B., Strada, E., Tuzzi, E., Verosub, K., Wilson, G., Wilson, T., Wonik, T. and Zattin, M.: Antarctic
920 ice sheet sensitivity to atmospheric CO₂ variations in the early to mid-Miocene, *Proc. Natl. Acad. Sci. U.*
921 *S. A.*, 113(13), 3453–3458, doi:10.1073/pnas.1516030113, 2016.

922 Lewis, A. R., Marchant, D. R., Ashworth, A. C., Hedenas, L., Hemming, S. R., Johnson, J. V., Leng, M. J.,
923 Machlus, M. L., Newton, A. E., Raine, J. I., Willenbring, J. K., Williams, M. and Wolfe, A. P.: Mid-
924 Miocene cooling and the extinction of tundra in continental Antarctica, *Proc. Natl. Acad. Sci.*, 105(31),
925 10676–10680, doi:10.1073/pnas.0802501105, 2008.

926 Lifton, N., Sato, T. and Dunai, T. J.: Scaling in situ cosmogenic nuclide production rates using analytical
927 approximations to atmospheric cosmic-ray fluxes, *Earth Planet. Sci. Lett.*, 386, 149–160,
928 doi:10.1016/j.epsl.2013.10.052, 2014.

929 Lisiecki, L. E. and Raymo, M. E.: A Pliocene-Pleistocene stack of 57 globally distributed benthic $\delta^{18}O$ records,
930 *Paleoceanography*, 20, 1–17, doi:10.1029/2004PA001071, 2005.

931 Margerison, H. R., Phillips, W. M., Stuart, F. M. and Sugden, D. E.: Cosmogenic 3He concentrations in ancient
932 flood deposits from the Coombs Hills, northern Dry Valleys, East Antarctica: Interpreting exposure ages
933 and erosion rates, *Earth Planet. Sci. Lett.*, 230, 163–175, doi:10.1016/j.epsl.2004.11.007, 2005.

934 Mayewski, P. A.: Glacial geology and late Cenozoic history of the Transantarctic Mountains, Antarctica., Ph.D.
935 Thesis, Institute of Polar Studies, The Ohio State University, United States of America, 1975.

936 [Mercer, J.H., 1968. Glacial geology of the Reedy glacier area, Antarctica. *Geological Society of America Bulletin*](#)
937 [79, 471-486.](#)

938 Mercer, J. H.: Some observations on the glacial geology of the Beardmore Glacier area, *Antarct. Geol. Geophys.*,
939 (427–433), 1972.

940 Middleton, J. L., Ackert, R. P. and Mukhopadhyay, S.: Pothole and channel system formation in the McMurdo Dry
941 Valleys of Antarctica: New insights from cosmogenic nuclides, *Earth Planet. Sci. Lett.*, 355–356, 341–350,
942 doi:10.1016/j.epsl.2012.08.017, 2012.

943 Miller, K. G., Kominz, M. A., Browning, J. V., Wright, J. D., Mountain, G. S., Katz, M. E., Sugarman, P. J.,
944 Cramer, B. S., Christie-Blick, N. and Pekar, S. F.: The Phanerozoic record of global sea-level change,
945 *Science*, 310, 1293–1298, doi:10.1126/science.1116412, 2005.

946 Miller, S. R., Fitzgerald, P. G. and Baldwin, S. L.: Cenozoic range-front faulting and development of the
947 Transantarctic Mountains near Cape Surprise, Antarctica: Thermochronologic and geomorphologic
948 constraints, *Tectonics*, 29(1), 1–21, doi:10.1029/2009TC002457, 2010.

949 Nishiizumi, K.: Preparation of ^{26}Al AMS standards, *Nucl. Instruments Methods Phys. Res. Sect. B Beam Interact.*
950 *with Mater. Atoms*, 223–224, 388–392, doi:10.1016/j.nimb.2004.04.075, 2004.

951 Nishiizumi, K., Imamura, M., Caffee, M. W., Southon, J. R., Finkel, R. C. and McAninch, J.: Absolute calibration of
952 ^{10}Be AMS standards, *Nucl. Instruments Methods Phys. Res. Sect. B Beam Interact. with Mater. Atoms*,
953 258, 403–413, doi:10.1016/j.nimb.2007.01.297, 2007.

954 [Orombelli, G., Baroni, C., Denton, G.H., 1990. Late Cenozoic glacial history of the Terra Nova Bay region, northern](#)
955 [Victoria Land, Antarctica. *Geografica Fisica e Dinamica Quaternaria* 13, 139-163.](#)

956 Pagani, M., Liu, Z., Lariviere, J. and Ravelo, A. C.: High Earth-system climate sensitivity determined from Pliocene
957 carbon dioxide concentrations, *Nat. Geosci.*, 3, 27–30, doi:10.1038/ngeo724, 2010.

958 Phillips, F. M., Argento, D. C., Balco, G., Caffee, M. W., Clem, J., Dunai, T. J., Finkel, R., Goehring, B., Gosse, J.
959 C., Hudson, A. M., Jull, A. J. T., Kelly, M. A., Kurz, M., Lal, D., Lifton, N., Marrero, S. M., Nishiizumi,
960 K., Reedy, R. C., Schaefer, J., Stone, J. O. H., Swanson, T. and Zreda, M. G.: Quaternary Geochronology
961 The CRONUS-Earth Project : A synthesis, *Quat. Geochronol.*, 31, 119–154, 2016.

962 Pollard, D. and DeConto, R. M.: Contribution of Antarctica to past and future sea-level rise, *Nature*, 531, 591–597,
963 doi:10.1038/nature17145, 2016.

964 Pollard, D., DeConto, R. M. and Alley, R. B.: Potential Antarctic Ice Sheet retreat driven by hydrofracturing and ice
965 cliff failure, *Earth Planet. Sci. Lett.*, 412, 112–121, doi:10.1016/j.epsl.2014.12.035, 2015.

966 Prentice, M. L., Denton, G. H., Lowell, T. V., Conway, H. C. and Heusser, L. E.: Pre-late Quaternary glaciation of
967 the Beardmore glacier region, Antarctica, *Antarct. J. United States*, 21, 95–98, 1986.

968 Railsback, L. B., Gibbard, P. L., Head, M. J., Voarintsoa, N. R. G. and Toucanne, S.: An optimized scheme of
969 lettered marine isotope substages for the last 1.0 million years, and the climatostratigraphic nature of
970 isotope stages and substages, *Quat. Sci. Rev.*, 111, 94–106, doi:10.1016/j.quascirev.2015.01.012, 2015.

971 Rovere, A., Raymo, M. E., Mitrovica, J. X., Hearty, P. J., O’Leary, M. J., Inglis, J. D., Leary, M. J. O. and Inglis, J.
972 D.: The Mid-Pliocene sea-level conundrum: Glacial isostasy, eustasy and dynamic topography, *Earth
973 Planet. Sci. Lett.*, 387, 27–33, doi:10.1016/j.epsl.2013.10.030, 2014.

974 Scambos, T. A., Haran, T. M., Fahnestock, M. A., Painter, T. H. and Bohlander, J.: MODIS-based Mosaic of
975 Antarctica (MOA) data sets: Continent-wide surface morphology and snow grain size, *Remote Sens.
976 Environ.*, 111, 242–257, doi:10.1016/j.rse.2006.12.020, 2007.

977 Schaefer, J. M., Ivy-Ochs, S., Wieler, R., Leya, I., Baur, Denton, G. H. and Schluchter, C.: Cosmogenic noble gas
978 studies in the oldest landscape on Earth: surface exposure age of the Dry Valleys, Antarctica, *Earth Planet.
979 Sci. Lett.*, 167, 215–226, 1999.

980 Schaefer, J. M., Denton, G. H., Kaplan, M., Putnam, A., Finkel, R. C., Barrell, D. J. A., Andersen, B. G., Schwartz,
981 R., Mackintosh, A., Chinn, T. and Schluchter, C.: High-frequency Holocene glacier fluctuations in New
982 Zealand differ from the northern signature, *Science*, 324, 622–625, doi:10.1126/science.1169312, 2009.

983 Scherer, R. P., DeConto, R. M., Pollard, D. and Alley, R. B.: Windblown Pliocene diatoms and East Antarctic Ice
984 Sheet retreat, *Nat. Commun.*, 7, 1–9, doi:10.1038/ncomms12957, 2016.

985 Seki, O., Foster, G. L., Schmidt, D. N., Mackensen, A., Kawamura, K. and Pancost, R. D.: Alkenone and boron-
986 based Pliocene pCO₂ records, *Earth Planet. Sci. Lett.*, 292, 201–211, doi:10.1016/j.epsl.2010.01.037, 2010.

987 Shevenell, A. E., Kennett, J. P. and Lea, D. W.: Middle Miocene ice sheet dynamics, deep-sea temperatures, and
988 carbon cycling: A Southern Ocean perspective, , doi:10.1029/2007GC001736, 2008.

989 Sosdian, S. M., Greenop, R., Hain, M. P., Foster, G. L., Pearson, P. N. and Lear, C. H.: Constraining the evolution
990 of Neogene ocean carbonate chemistry using the boron isotope pH proxy, *Earth Planet. Sci. Lett.*, 498,
991 362–376, doi:10.1016/j.epsl.2018.06.017, 2018.

992 Spector, P., Stone, J., Cowdery, S. G., Hall, B., Conway, H. and Bromley, G.: Rapid early-Holocene deglaciation in
993 the Ross Sea, Antarctica, *Geophys. Res. Lett.*, 44(15), 7817–7825, doi:10.1002/2017GL074216, 2017.

994 [Stern, T. A., ten Brink, U.S.: Flexural Uplift of the Transantarctic Mountains, *J. Geophys. Res.*, 94\(B8\), 10,315-](#)
995 [10,330, 1989.](#)

996 Stern, T. A., Baxter, A. K. and Barrett, P. J.: Isostatic rebound due to glacial erosion within the Transantarctic
997 Mountains, *Geology*, 33(3), 221–224, doi:10.1130/G21068.1, 2005.

998 Stone, J. O.: Air pressure and cosmogenic isotope production, *J. Geophys. Res.*, 105(B10), 23753–59, 2000.

999 Stone, J. O., Balco, G., Sugden, D. E., Caffee, M. W., Sass, L. C. I., Cowdery, S. G. and Siddoway, C.: Holocene
1000 Deglaciation of Marie Byrd Land, West Antarctica, *Science*, 299(5603), 99–102,
1001 doi:10.1126/science.1115233, 2003.

1002 Strasky, S., Di Nicola, L., Baroni, C., Salvatore, M. C., Baur, H., Kubik, P. W., Schlüchter, C. and Wieler, R.:
1003 Surface exposure ages imply multiple low-amplitude Pleistocene variations in East Antarctic Ice Sheet,
1004 Ricker Hills, Victoria Land, *Antarct. Sci.*, 21(1), 59–69, doi:10.1017/S0954102008001478, 2009.

1005 Sugden, D. and Denton, G.: Cenozoic landscape evolution of the Convoy Range to Mackay Glacier area,
1006 Transantarctic Mountains: Onshore to offshore synthesis, *Bull. Geol. Soc. Am.*, 116(7–8), 840–857,
1007 doi:10.1130/B25356.1, 2004.

1008 Sugden, D. E. , Marchant, D. R. . and Denton, G. H. .: The Case for a Stable East Antarctic Ice Sheet, *Geogr. Ann.*
1009 *Ser. A Phys. Geogr.*, 75(4), 151–154, 1993.

1010 Swanger, K. M., Marchant, D. R., Schaefer, J. M., Winckler, G. and Head, J. W.: Elevated East Antarctic outlet
1011 glaciers during warmer-than-present climates in southern Victoria Land, *Glob. Planet. Change*, 79, 61–72,
1012 doi:10.1016/j.gloplacha.2011.07.012, 2011.

1013 Todd, C., Stone, J., Conway, H., Hall, B. and Bromley, G.: Late Quaternary evolution of Reedy Glacier, Antarctica,
1014 *Quat. Sci. Rev.*, 29(11–12), 1328–1341, doi:10.1016/j.quascirev.2010.02.001, 2010.

1015 Vermeesch, P., Balco, G., Blard, P. H., Dunai, T. J., Kober, F., Niedermann, S., Shuster, D. L., Strasky, S., Stuart, F.
1016 M., Wieler, R. and Zimmermann, L.: Interlaboratory comparison of cosmogenic²¹Ne in quartz, *Quat.*
1017 *Geochronol.*, 26(1), 20–28, doi:10.1016/j.quageo.2012.11.009, 2015.

1018 De Vleeschouwer, D., Vahlenkamp, M., Crucifix, M. and Pälike, H.: Alternating Southern and Northern
1019 Hemisphere climate response to astronomical forcing during the past 35 m.y, *Geology*, 45(4), 375–378,
1020 doi:10.1130/G38663.1, 2017.

Deleted: 23,

1022 Wang, Y., Momohara, A., Wang, L., Lebreton-Anberrée, J. and Zhou, Z.: Evolutionary history of atmospheric CO₂
1023 during the late cenozoic from fossilized metasequoia needles, *PLoS One*, 10(7), 1–15,
1024 doi:10.1371/journal.pone.0130941, 2015.

1025 Van der Wateren, F. M., Dunai, T. J., Van Balen, R. T., Klas, W., Verbers, A. L. L. M., Passchier, S. and Hergers,
1026 U.: Contrasting neogene denudation histories of different structural regions in the transantarctic mountains
1027 rift flank constrained by cosmogenic isotope measurements, *Glob. Planet. Change*, (23), 145–172, 1999.

1028 Webb, P. N., Harwood, D. M., McKelvey, B. C., Mercer, J. H. and Stott, L. D.: Cenozoic marine sedimentation and
1029 ice-volume variation on the East Antarctic craton., *Geology*, 12, 287–291, doi:10.1130/0091-
1030 7613(1984)12<287:CMSAIV>2.0.CO;2, 1984.

1031 Wilch, T. I., Lux, D. R., Denton, G. H. and McIntosh, W. C.: Minimal Pliocene-Pleistocene uplift of the dry valleys
1032 sector of the Transantarctic Mountains: a key parameter in ice-sheet reconstructions, *Geology*, 21(9), 841–
1033 844, doi:10.1130/0091-7613(1993)021<0841:MPPUOT>2.3.CO;2, 1993.

1034 Willeit, M., Ganopolski, A., Calov, R. and Brovkin, V.: Mid-Pleistocene transition in glacial cycles explained by
1035 declining CO₂ and regolith removal, *Sci. Adv.*, 5(4), 1–8, doi:10.1126/sciadv.aav7337, 2019.

1036 Winnick, M. J. and Caves, J. K.: Oxygen isotope mass-balance constraints on Pliocene sea level and East Antarctic
1037 Ice Sheet stability, *Geology*, 43(10), 879–882, doi:10.1130/G36999.1, 2015.

1038 Zhang, Y. G. Y. G., Pagani, M., Liu, Z., Bohaty, S. M. S. M. and DeConto, R.: A 40-million-year history of
1039 atmospheric CO₂, *Philos. Trans. R. Soc. A*, 371, 1–20, 2013.

1040

Deleted: D

